



Publication Year	2016
Acceptance in OA @INAF	2020-04-30T14:00:58Z
Title	Testing the Asteroseismic Scaling Relations for Red Giants with Eclipsing Binaries Observed by Kepler
Authors	Gaulme, P.; McKeever, J.; Jackiewicz, J.; Rawls, M. L.; CORSARO, ENRICO MARIA NICOLA; et al.
DOI	10.3847/0004-637X/832/2/121
Handle	http://hdl.handle.net/20.500.12386/24375
Journal	THE ASTROPHYSICAL JOURNAL
Number	832



TESTING THE ASTEROSEISMIC SCALING RELATIONS FOR RED GIANTS WITH ECLIPSING BINARIES OBSERVED BY *KEPLER*

P. GAULME^{1,2}, J. MCKEEVER¹, J. JACKIEWICZ¹, M. L. RAWLS¹, E. CORSARO^{3,4,5}, B. MOSSER⁶,

J. SOUTHWORTH⁷, S. MAHADEVAN^{8,9}, C. BENDER^{8,9}, AND R. DESHPANDE^{8,9}

¹ Department of Astronomy, New Mexico State University, P.O. Box 30001, MSC 4500, Las Cruces, NM 88003-8001, USA; gaulme@nmsu.edu

² Apache Point Observatory, 2001 Apache Point Road, P.O. Box 59, Sunspot, NM 88349, USA

³ Laboratoire AIM, CEA/DRF-CNRS, Université Paris 7 Diderot, IRFU/SAP, Centre de Saclay, F-91191 Gif-sur-Yvette, France

⁴ Instituto de Astrofísica de Canarias, E-38200 La Laguna, Tenerife, Spain

⁵ Departamento de Astrofísica, Universidad de La Laguna, E-38205 La Laguna, Tenerife, Spain

⁶ LESIA, Observatoire de Paris, PSL Research University, CNRS, Université Pierre et Marie Curie, Université Denis Diderot, F-92195 Meudon, France

⁷ Astrophysics Group, Keele University, Staffordshire, ST5 5BG, UK

⁸ Department of Astronomy & Astrophysics, The Pennsylvania State University, 525 Davey Lab, University Park, PA 16802, USA

⁹ Center for Exoplanets & Habitable Worlds, The Pennsylvania State University, 525 Davey Lab, University Park, PA 16802, USA

Received 2016 May 18; revised 2016 September 15; accepted 2016 September 16; published 2016 November 22

ABSTRACT

Given the potential of ensemble asteroseismology for understanding fundamental properties of large numbers of stars, it is critical to determine the accuracy of the scaling relations on which these measurements are based. From several powerful validation techniques, all indications so far show that stellar radius estimates from the asteroseismic scaling relations are accurate to within a few percent. Eclipsing binary systems hosting at least one star with detectable solar-like oscillations constitute the ideal test objects for validating asteroseismic radius and mass inferences. By combining radial velocity (RV) measurements and photometric time series of eclipses, it is possible to determine the masses and radii of each component of a double-lined spectroscopic binary. We report the results of a four-year RV survey performed with the échelle spectrometer of the Astrophysical Research Consortium's 3.5 m telescope and the APOGEE spectrometer at Apache Point Observatory. We compare the masses and radii of 10 red giants (RGs) obtained by combining radial velocities and eclipse photometry with the estimates from the asteroseismic scaling relations. We find that the asteroseismic scaling relations overestimate RG radii by about 5% on average and masses by about 15% for stars at various stages of RG evolution. Systematic overestimation of mass leads to underestimation of stellar age, which can have important implications for ensemble asteroseismology used for Galactic studies. As part of a second objective, where asteroseismology is used for understanding binary systems, we confirm that oscillations of RGs in close binaries can be suppressed enough to be undetectable, a hypothesis that was proposed in a previous work.

Key words: binaries: eclipsing – stars: evolution – stars: oscillations

Supporting material: machine-readable table

1. OSCILLATING RED GIANTS IN ECLIPSING BINARIES

The simplest analysis of asteroseismic data is based on the overall properties of the oscillations, which are the frequency of their maximum amplitude ν_{\max} and the mean frequency separation $\Delta\nu$ between consecutive modes of the same degree. Thanks to the pair of asteroseismic scaling relations and a measurement of effective temperature T_{eff} , one gets an estimate of a star's surface gravity $\log g$ and mean density $\bar{\rho}$ by respectively comparing ν_{\max} and $\Delta\nu$ with those of the Sun (e.g., Kjeldsen & Bedding 1995):

$$\frac{\bar{\rho}}{\bar{\rho}_{\odot}} = \left(\frac{\Delta\nu}{\Delta\nu_{\odot}} \right)^2 \quad (1)$$

$$\frac{g}{g_{\odot}} = \frac{\nu_{\max}}{\nu_{\max_{\odot}}} \left(\frac{T_{\text{eff}}}{T_{\text{eff}_{\odot}}} \right)^{\frac{1}{2}}. \quad (2)$$

It is then straightforward to deduce a star's mass M and radius R relative to the Sun:

$$\frac{R}{R_{\odot}} = \left(\frac{\nu_{\max}}{\nu_{\max_{\odot}}} \right) \left(\frac{\Delta\nu_{\odot}}{\Delta\nu} \right)^2 \left(\frac{T_{\text{eff}}}{T_{\text{eff}_{\odot}}} \right)^{\frac{1}{2}} \quad (3)$$

$$\frac{M}{M_{\odot}} = \left(\frac{\nu_{\max}}{\nu_{\max_{\odot}}} \right)^3 \left(\frac{\Delta\nu_{\odot}}{\Delta\nu} \right)^4 \left(\frac{T_{\text{eff}}}{T_{\text{eff}_{\odot}}} \right)^{\frac{3}{2}}. \quad (4)$$

In practice, the measurement of the asteroseismic global parameters ν_{\max} and $\Delta\nu$ has been largely used to estimate masses and radii of the stars displaying solar-like oscillations from the CoRoT and *Kepler* data (see Belkacem et al. 2013; Chaplin & Miglio 2013, for recent reviews).

Given the importance of asteroseismology and its scaling laws, much effort has been carried out to test their validity. We may distinguish two kinds of approaches: those based on validating the relation between $\Delta\nu$ and mean density $\bar{\rho}$ from models and simulated data (e.g., Stello et al. 2009; White et al. 2011; Miglio et al. 2013) and others based on measuring R of actual stars independent of asteroseismology (e.g., Huber et al. 2011, 2012; Silva Aguirre et al. 2012; Baines et al. 2014). All works indicated that radius estimates from asteroseismic scaling relations are accurate to a few percent. On the contrary, similar tests with independent mass determination of oscillating stars for individual stars have not been possible so far. Indeed, theoretical studies focused on the reliability of the $\Delta\nu$ – $\bar{\rho}$ scaling relation and not on ν_{\max} . This is because ν_{\max} has no secure theoretical basis, as it is not yet possible to make reliable

predictions of the amplitude of stochastically excited modes and their dependence on frequency (Belkacem et al. 2011; Christensen-Dalsgaard 2012). Observationally, there is some evidence to support the conclusion that the scaling relations do provide biased masses in some instances. Epstein et al. (2014) have found that the masses of metal-poor halo giants are significantly overestimated. White et al. (2013) found that combining the interferometric radii with the asteroseismic density implied a mass for the F star θ Cyg that was significantly lower than expected from its position in the Hertzsprung–Russell diagram.

Eclipsing binary systems (EBs) hosting at least one star with detectable solar-like oscillations constitute an ideal test case. Indeed, it is possible to determine the projected masses of each component ($M_1 \sin i$, $M_2 \sin i$) for double-line spectroscopic binaries (SB2) and the mass function $M_2^3/(M_1 + M_2)^2 \sin^3 i$ for single-line spectroscopic binaries (SB1), where i is the inclination of the orbital plane. For EBs, the inclination i is easily retrieved from modeling the eclipses in the light curves. Absolute stellar radii (R_1 , R_2) are obtained from combining radial velocity (RV) and eclipse photometric measurements.

So far, all published stars known to both display solar-like oscillations and belong to EBs are red giants (RGs), and all have been detected by the *Kepler* mission. The first detection was the system KIC 8410637 with a 408-day period (Hekker et al. 2010; Frandsen et al. 2013). Since then, Gaulme et al. (2013, 2014) reported a list 18 RG eclipsing-binary (RG/EB) candidates, of which 14 displayed oscillations. Beck et al. (2014, 2015) reported the discovery of 17 stars with tidally excited pulsations (“heart-beat”), where each system has an RG component with oscillations, and two are also EBs. Two RG/EB systems, KIC 8410637 and 9246715, have been completely characterized in terms of masses and radii by combining photometry and radial velocities (Frandsen et al. 2013; Helminiak et al. 2015; Rawls et al. 2016). Both show a fairly good agreement between asteroseismic and dynamical estimates of surface gravities and mean densities, even though Huber (2014) and Brogaard et al. (2016) contested the agreement regarding KIC 8410637.

Gaulme et al. (2014) observed that, among the 19 RG/EBs identified at the time, four systems did not display oscillations. This is observed in the closest systems where rotational and orbital periods are almost synchronized and where strong surface activity is detected. They suggested that tidal forces, which tend to synchronize and circularize binary systems, spin up RGs, with this phenomenon becoming stronger as systems are closer. This would lead to the development of a dynamo mechanism and thus the generation of magnetic fields in the RGs that become visible at the surface. The resulting spots likely absorb part of the pressure mode energy, making oscillations impossible to detect in the closest systems. Alternatively, it is proposed that the presence of spots shows that the convective energy is diverted into the activity signal and not into global oscillations. This would mean that the properties of convection are considerably affected by binarity in the closest systems, and that oscillation excitation is reduced or suppressed altogether.

In this paper, we report the results of a four-year RV survey performed with the échelle spectrometer of the Astrophysical Research Consortium (ARC) 3.5 m telescope at Apache Point Observatory (APO). We benefited from complementary observations by the Apache Point Observatory Galactic Evolution Experiment (APOGEE) spectrograph for one system. The targets are 17 EB systems of the 18 Gaulme et al.

(2013, 2014) RG/EB candidates, whose orbital periods range from 15 to 1,058 days. Among those, solar-like oscillations are detected in 13, of which nine are SB2s and four SB1s. The remaining four are RG/EB candidates where no oscillations are detected. Our first objective is to test the nature of the 17 systems, where RVs allow us to determine whether the RGs belong to or are aligned with EBs. The second consists of measuring the masses and radii of the four RG candidates with no oscillations to determine if their expected ν_{\max} fall in the observable range, that is, not much larger than the Nyquist frequency. The third and main objective is the comparison of masses, radii, mean densities, and surface gravities with those obtained with the asteroseismic scaling relations. For the latter, we consider the nine SB2 with oscillations as well as KIC 8410637, for which we reestimate its asteroseismic parameters and use the Frandsen et al. (2013) dynamical measurement of the mass and radius of each star.

2. DATA AND ANALYSIS

2.1. Kepler Photometric Light Curves

Light curves are used for a double purpose—eclipse and asteroseismic modeling—which entails modeling eclipse shapes by removing stellar activity and measuring solar-like oscillations by removing eclipse features. The methods we use are described in Gaulme et al. (2013, 2014), and here we provide a summary. The way light curves are processed is of prime importance because part of the conclusions of this paper depends on our ability to provide reliable estimates of stellar radii. As we indicate in Section 2.3, radii measurements are a function of the relative depths of the eclipses, unlike mass, which is not sensitive to eclipse photometry. We thus need the relative photometry to be calibrated as finely as possible.

We work with the raw SAP_FLUX measurements, which are the fluxes integrated per mask aperture, available on the MAST web site.¹⁰ The major challenge in concatenating light curves and studying stellar activity on periods longer than a quarter is to ensure photometric continuity before and after each interruption. The main cause of photometric jumps from quarter to quarter is the fact that the *Kepler* telescope rotates four times a year, which implies that a given star falls on four different chips. However, the pointing is fine enough that a star repeatedly covers the same group of pixels every fourth quarter. Light curves are obtained by adding the pixels of the masks that are designed for every star in the field of view. For a given star, a mask is designed for each of *Kepler*’s positions. Because of the photo response nonuniformity (PRNU) of the pixels and the changing size of the masks, the recorded flux changes. Both PRNU and varying mask areas lead to a flux discontinuity that should be adjusted in a multiplicative way. The first correction we apply is therefore a normalization that turns the photoelectric counts into relative flux, by dividing each quarter’s light curve by its average. A median is actually more appropriate than a mean as outliers and large photometric jumps can bias the mean. If photometric variations would only be generated by PRNU and masks, this process should be enough. As a matter of fact, this is true for systems where no stellar activity is measurable, if we exclude the effect of the differential velocity aberration (see below).

¹⁰ <http://archive.stsci.edu/kepler/>

Issues arise with the systems that display strong pseudoperiodic luminosity fluctuations. For those, the average (or median) over a quarter is biased by the fact that the number of pseudoperiods is too small to be averaged out. In our cases, pseudoperiods range from 15 to about 60 days. Therefore, the median is not a perfect estimator of the mean photometry. This is an intrinsic limitation of the light curve photometric accuracy. In such cases, jumps remain, of amplitudes within a few percent. Given that the remaining jumps are caused by a biased normalization, the second layer of adjustment to be applied should still be done in a multiplicative way. However, this is not possible in practice because none of the quarters can be considered as an absolute reference. The only corrections we may apply are additive, to ensure a smooth aspect of the light curve and to minimize their effects in the Fourier domain. This explains why residuals are larger when modeling systems with large photometric activity (KIC 7943602, 3955867, 4569590, and 9291629; see Figure 3). When modeling such systems, what matters is that the residuals are symmetrically distributed around the best model light curve. Note that this discussion regards mostly the systems with no oscillations and does not have any significant impact on the systems used to test the asteroseismic scaling laws.

We employ two ways to smooth the remaining discontinuities once quarters are divided by their median. When a gap is short with respect to the photometric variability timescale, each side of the gap is adjusted accordingly. When a gap is longer than the variability period, we simply adjust the photometry with the difference of the means of each chunk surrounding the gap. Once the complete time series is leveled and concatenated, a linear fit is subtracted from it to take into account the decreasing instrumental sensitivity. Finally, we compensate for the differential velocity aberration—the motion of the target across a fixed aperture smaller than the point-spread function—caused by the pixel scale breathing along the satellite’s orbit (372.5 days), whose peak-to-peak amplitude ranges from 0.5% to 3.8%. This is done by subtracting from each light curve a 372.5 day period sine fitting and a first harmonic, which is enough to reduce its amplitude to less than 0.5%.

For asteroseismic analysis, we remove the data corresponding to the eclipses and bridge them with a second-order polynomial, constrained by the surrounding data. We then smooth the eclipse-less light curve on a large number of points (about 1,000) and subtract it from the original, clean light curve to get a flattened time series, which we use for eclipse modeling.

For asteroseismology we work with the power density spectra of the light curves. To minimize the effects of the incomplete duty cycle, we perform gap fillings and make use of the fast Fourier transform. All short gaps (only several missing points) are interpolated with a second-order polynomial estimated from the nearby data points. Long gaps are filled with zeros. To reduce the impact of abrupt discontinuities around long gaps, the edges of each section in between gaps are apodized with a cosine function. This is particularly important when significant variability is detected. Overall, the duty cycle for these objects is always greater than 85%.

2.2. Spectroscopy and Stellar Parameters

All spectra were obtained with the échelle spectrometer of the 3.5 m ARC telescope at APO (ARCES), except a set of 25 spectra of the system KIC 7037405 from the APOGEE spectrometer of the Sloan Digital Sky Survey (SDSS; Eisenstein et al. 2011), also based at APO. Details on how

the RVs were determined from the ARC échelle spectra are described in Rawls et al. (2016). As regards APOGEE, we followed the procedures described in Bender et al. (2012) and S. Mahadevan et al. (2016, in preparation). In brief, we start with the extracted and wavelength-calibrated “visit” spectra produced by the APOGEE data-reduction pipeline (Nidever et al. 2015). These spectra are further cleaned of processing residuals resulting from incomplete corrections by the pipeline of telluric absorption and OH emission features, and continuum normalized. We do not utilize the pipeline-derived RVs but instead use one-dimensional and two-dimensional cross-correlation analysis against template spectra, through a customized implementation of the TODCOR algorithm (Mazeh & Zucker 1994). Templates are constructed from the PHOENIX-based BT-Settl model (Allard et al. 2011) corresponding to the APOGEE-derived T_{eff} , $\log g$, and $[M/H]$, convolved to the APOGEE spectral resolution of 22,500 and rotationally broadened using a four-parameter nonlinear limb-darkening model (Claret et al. 2012). RV measurements are provided in the Appendix.

To determine stellar atmospheric parameters from ARCES data, individual spectra for each object were coadded after removing the derived RV shift due to the motion of the RG at each epoch. The resulting composite spectrum has a higher signal-to-noise ratio (S/N) and ignores the contribution of the companion star, whose flux is typically a few percent of the total. While this should certainly remove the spectral lines of the companion (which has a different RV than the RG), there should still be a contribution from the continuum. By assuming all lines are equally damped—that is, the effect of the continuum is felt equally across the entire spectrum—then the net effect is a shift in the abundance. Thus, a dilution of lines (smaller measured EW) leads to a lower abundance estimation.

We used the MOOG spectral synthesis code (Sneden et al. 2012) to derive the spectroscopic parameters T_{eff} , $\log g$, $[Fe/H]$, and microturbulence of the RG star. The technique assumes LTE to achieve ionization and excitation balance for iron lines in the stellar spectrum. This is done using the equivalent width (EW) of the iron lines and an appropriate atmosphere model. In our case, we used a grid of Kurucz ATLAS9 plane-parallel model atmospheres (Castelli & Kurucz 2004). A review of the process can be found in Sousa (2014). We use a set of 120 Fe I lines and 17 Fe II lines optimized for cool stars (Tsantaki et al. 2013). The EWs in our spectra were measured using the automated EW finder ARES (Sousa et al. 2007, 2015). A visual inspection of the output from ARES was performed to ensure that only clear and easily visible lines were included in the rest of the analysis. We follow the algorithm outlined in Magrini et al. (2013) to quickly arrive at the best solution and associated errors.

The derived spectroscopic parameters are provided in Table 1. Figure 1 compares these values with other published results from various catalogs, such as the *Kepler* Input Catalog and the APOKASC catalog. In Figure 2, we specifically compare the measurements using visible spectra and APOGEE infrared spectra. The visible spectra have systematically larger T_{eff} values, as well as lower metallicities, with the discrepancy increasing for more metal-rich stars. The $\log g$ values show better agreement within the uncertainties. We choose to use only the atmospheric parameters we retrieve from the ARCES visible spectra, instead of APOGEE’s, for two reasons. First, APOGEE spectra are available for only about half of the

Table 1
Atmospheric Parameters of the Red Giants from the ARC 3.5 m Visible Spectra

KIC	m_{Kep}	ARCES			APOGEE		
		T_{eff} (K)	$\log g$ (dex)	[Fe/H] (dex)	T_{eff} (K)	$\log g$ (dex)	[Fe/H] (dex)
3955867	13.55	4884(83)	3.2(2)	−0.55(4)	4623(91)	3.0(1)	−0.53(5)
4569590	12.80	4706(152)	2.5(4)	−0.34(9)
4663623	12.83	4812(92)	2.7(2)	−0.13(6)	4803(91)	2.7(1)	0.16(4)
5179609	12.78	5003(54)	3.7(2)	0.22(7)	4887(91)	3.3(1)	0.45(4)
5308778	11.78	4900(44)	2.5(2)	−0.43(2)	5044(91)	3.3(1)	−0.23(4)
5786154	13.53	4747(100)	2.6(2)	−0.06(6)
7037405	11.88	4516(36)	2.5(2)	−0.34(1)	4542(91)	2.3(1)	−0.13(6)
7377422	13.56	4938(110)	3.1(2)	−0.33(6)
8054233	11.78	4971(90)	2.8(2)	−0.15(5)
8410637	10.77	4699(91)	2.7(1)	0.16(3)
8430105	10.42	5042(68)	3.04(9)	−0.49(4)	4918(91)	3.0(1)	−0.43(8)
8702921	11.98	5058(86)	3.3(2)	0.15(5)	4958(91)	3.3(1)	0.44(6)
9246715	9.27	5030(45)	3.0(2)	0.05(2)
9291629	13.96	4713(151)	3.4(3)	0.04(6)
9540226	11.67	4692(65)	2.2(2)	−0.33(4)	4662(91)	2.5(1)	−0.16(8)
9970396	11.45	4916(68)	3.1(1)	−0.23(3)	4789(91)	2.7(1)	−0.18(7)
10001167	10.05	4700(66)	2.6(1)	−0.69(4)	4539(91)	2.3(1)	−0.7(2)

Note. APOGEE estimates from the DR12 release are indicated in the last three columns when available. Systems are sorted by increasing KIC number.

systems, and we prefer to work with a consistent set of temperatures obtained from the same instrument and data processing routines. Second, even though APOGEE data are less sensitive to the companion's line, the data are processed in a massive automatic pipeline, while we worked with the ARCES spectra one-by-one. To confirm that our results are of good quality, we tested the method on well-known RGs that we also observed with ARCES to calibrate our method. Finally, when comparing our temperature estimates with those available in the literature (Figure 1), our measurements are very consistent with the average of what was obtained independently.

2.3. Physical Properties from Eclipses and Radial Velocities

Eclipse modeling consists of retrieving the physical parameters of a binary system from the eclipse duration, depth, and shape. These systems are composed of an RG and a companion that is usually a main-sequence star. In this paper, as well as in Gaulme et al. (2013, 2014), we make the sacrilegious choice of defining the primary eclipse to be that where the companion star passes in front of the RG. The reason is that all of our systems but KIC 9246715 (discussed in the present work but analyzed in Rawls et al. 2016) are composed of a small companion and an RG, which makes the exoplanet terminology easier to use: primary or secondary refers to the radius instead of the temperature ratio. Thus, for cases composed of a Sun-like main-sequence star and a cooler but larger RG, secondary eclipses are deeper than primary ones. Regarding their shapes, primary eclipses are dominated by the RG limb-darkening function, whereas secondary eclipses are flat except during ingress and egress.

For a given system, we simultaneously fit the *Kepler* light curve and the RVs with the help of the JKTEBOP software (Southworth 2013). In the case of an SB2, JKTEBOP allows the retrieval of a system's orbital parameters (period, time and argument of periastron, eccentricity, inclination, semimajor axis) and stellar physical properties (masses, radii, temperature ratio). Semimajor axes, radii, and masses are deduced from a set of fitted parameters, which are the ratio of radii, the central

surface-brightness ratio, the sum of relative radii, limb darkening, inclination, amount of contamination by third light, time of one of the eclipses, semiamplitude, and offset of RVs. We fit the eccentricity e and argument of periastron ω through the set of parameters $e \cos \omega$ and $e \sin \omega$, which are less degenerate and provide more stable solutions. Since we work only with single-band photometry (*Kepler*), we have no robust constraint on the contamination factor, so we fix it at the mean value provided by the KIC (average over the four orientations of the satellite). All fitted parameters are displayed in Table 2.

Modeling the shape of the primary eclipse is highly dependent on the choice of the limb-darkening law of the stellar atmospheres. Indeed, limb darkening is correlated with the eclipse's impact parameter (a function of inclination), ratio of radii, and surface-brightness ratio. In our specific sample, companion stars are always much smaller than the RG ($R_{\text{cmp}}/R_{\text{RG}} < 0.23$), so the limb-darkening law of the companion has a negligible influence on the eclipse shapes. In fact, many fits fail because the limb-darkening parameters of the companion converge toward unphysical values (<0 or >1 at the limb). Therefore, we choose not to fit the limb darkening for the companion. Instead we get a first estimate of the limb darkening (quadratic law) with the JKTLD routine, and then subsequently only fit the first-order term for the RG. Among various options, JKTLD is able to provide a limb-darkening estimate corresponding to the *Kepler* bandpass by interpolating Sing (2010) coefficients.

As regards errors and noise, it is clear from the big scatter during the eclipse in Figures 3 and 4 that the dominant noise is systematic (due to the pulsations or spots) and not Poisson-like. The noise is thus correlated from point to point, on timescales of several hours. We therefore estimate the error bars on the fitted parameters with Task 9 in JKTEBOP, which takes as input a parameter file, finds the best fit, and then assesses the error bars on the parameters of the fit in a way that accounts for correlated noise. The residual-shift method is used, where the residuals around the best fit are shifted point-by-point through the observational data. After each shift a new best fit is calculated. Approximately 1,000 iterations were performed for each fit, which corresponds to shifts much longer than the

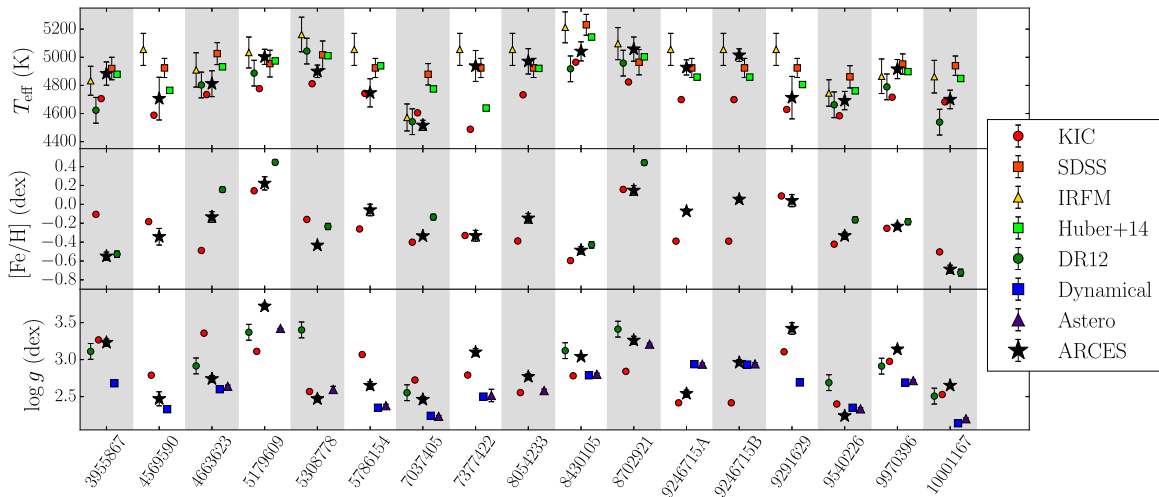


Figure 1. Comparisons of T_{eff} (top), $[\text{Fe}/\text{H}]$ (middle), and $\log g$ (bottom) from various sources to those derived by the spectroscopic analysis in this work (black stars). Photometrically derived values include *Kepler* Input Catalog as red circles (Brown et al. 2011), SDSS *griz* filter method as orange squares, infrared flux method (IRFM) values as yellow triangles (Pinsonneault et al. 2012), and revised KIC values as light green squares (Huber et al. 2014). Infrared spectroscopic values from DR12 of APOGEE are shown as green circles (Alam et al. 2015). Also indicated are the dynamically derived (blue squares) and asteroseismic (purple triangles) gravities.

oscillation or spot timescales. The 1σ errors are calculated by sorting the best fits and taking values that correspond to the central 68.3%. All models converged smoothly as all systems display total eclipses, except for KIC 5179609, where estimating its radius and temperature ratio was difficult.

For SB2s, the masses of both components are directly determined from the combined modeling of RV and photometric measurements. Note that masses can be estimated with good precision from RVs only for EBs with relatively distant stars ($\sin i \approx 1$). The mass of the RG is determined by the motion of the companion star, and vice versa. Since error bars on masses are related to the dispersion of RV measurements and the RG spectral lines display a much larger S/N, the precision on masses is better for companion stars than RGs. We obtain a median precision on RG masses of 3.35% (from 1.4% for 9970396 to 19.1% for 4663623) and 2.55% for companions (from 0.7% to 11.4%).

The relative precision on the radii is better than for the masses because of the exquisite quality of the *Kepler* light curves. There is no difference of precision for RGs and companions, and we report a median precision of 1.04% (from 0.4% to 5.1%). However, the accuracy of the radius measurements is lower than for masses as it depends on stellar atmospheric models, that is, limb darkening, which is not necessarily well constrained and can be the cause of small biases. Also, contamination from a third star in the aperture can affect the radius estimates through the ratio of the radii.

For most systems, we have fewer measurements of the companion’s Doppler shift since it is difficult to track its lines in the vicinity of eclipses. The median number of RV measurements for RG lines is 15.5 (from 12 to 44) and 13 for companions (from 7 to 19). The phase coverage is a function of the weather at APO and also of orbital periods. In addition, the two systems with the largest orbits (SB1 8054233 and SB2 4663623) were discovered about two years after the rest of the sample, resulting in poorer phase coverage and precision.

The four SB1 systems are worthy of discussion, despite not being suitable for testing asteroseismology. By assuming asteroseismology provides reliable RG masses and radii, it is possible to estimate the companion masses and radii. If the

Doppler shift is measured only for the RG, the relation

$$\frac{(M_2 \sin i)^3}{(M_1 + M_2)^2} = \frac{K_1^3 P (1 - e^2)^{3/2}}{2\pi G} \quad (5)$$

allows us to retrieve the companion’s mass, where M are stellar masses, the subscript 1 refers to the star for which we measure RVs, K_1 is the amplitude of the RV, and G is the gravitational constant. The mass ratio $q = M_2/M_1$ is one of the three roots of the equation

$$q^3 - \alpha q^2 - 2\alpha q - \alpha = 0, \quad (6)$$

where

$$\alpha = \frac{1}{2\pi G} \frac{K_1^3 P (1 - e^2)^{3/2}}{M_1 \sin^3 i}. \quad (7)$$

Note this method can be used to determine the mass M_2 of a planet transiting its host star, whose mass M_1 is estimated independently.

2.4. Physical Properties from Asteroseismic Scaling Relations and Mixed Modes

The stellar variability (star spots, granulation, and so on) is the cause of what is usually called the stellar “background” in the frequency domain. To determine the global asteroseismic parameters, we fit the background with a sum of two super Lorentzian functions centered on zero frequency, a Gaussian accounting for the mode envelope, and white noise. The center of the Gaussian function constitutes our measurement of ν_{max} . Given the importance of ν_{max} , both coauthors Gaulme and Corsaro independently fitted this parameter and found values that are fully compatible. Gaulme used a routine based on a Bayesian maximum a posteriori method (Gaulme et al. 2009), while Corsaro used the Bayesian DIAMONDS pipeline (Corsaro & Ridder 2014) following the methodology explained by Corsaro et al. (2015) and illustrated in Figure 5. The large frequency spacing $\Delta\nu_{\text{obs}}$ is obtained in two steps. We get a first estimate by measuring the maximum of the envelope of the autocorrelation of the time series filtered in the frequency range corresponding to the oscillations (Mosser &

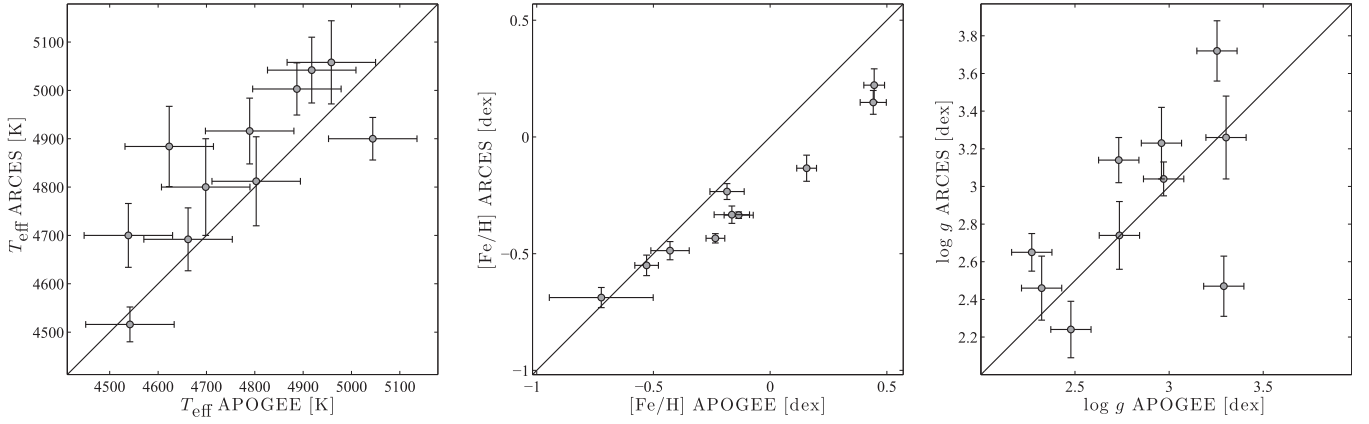


Figure 2. Comparison of the red giant atmospheric parameters (T_{eff} , $[\text{Fe}/\text{H}]$, $\log g$) obtained with ARCES (visible) and APOGEE (infrared) measurements.

Appourchaux 2009). However, the presence of many mixed $\ell = 1$ modes in RGs, which are not equally spaced in frequency, may bias autocorrelation methods. As a second step, we compared this first estimate with the so-called universal RG pattern, which should rectify any potential bias caused by $\ell = 1$ modes (Mosser et al. 2011). We are aware that measuring $\Delta\nu_{\text{obs}}$ by comparing the $\ell = 0$ frequencies to those predicted by the universal pattern erases any diversity that may exist in the RG oscillation spectra. Given that the objective of the present paper is to carefully compare masses and radii, we chose to reestimate all the global asteroseismic parameters, even though it was done by Gaulme et al. (2014). The main difference consists of two independent estimates of ν_{max} and the use of the universal RG pattern for $\Delta\nu$. Our estimates of ν_{max} and $\Delta\nu$ are displayed in Table 3.

The $\Delta\nu$ scaling relation comes from the fact that the oscillation pattern of low-degree pressure modes can be described by a second-order relation (Tassoul 1980). The first-order term shows that modes of a given degree are evenly spaced in frequency as a function of their radial order n . The second-order term is responsible for the curvature observed in the échelle diagrams used to analyze the oscillation spectra. This approximate relation that describes the mode frequencies is called asymptotic, since its derivation is strictly valid only for large n . The common use of asteroseismic scaling relations (e.g., Chaplin et al. 2011; White et al. 2012) neglects the curvature and assumes the large frequency spacing that is observed, $\Delta\nu_{\text{obs}}$, to be equal to the asymptotic large spacing $\Delta\nu_{\text{as}}$, for which the scalings are correct (but only in the case of homologous stars, e.g., Belkacem et al. 2013). In the case of RGs with $\nu_{\text{max}} \leq 50 \mu\text{Hz}$, the oscillations' radial orders are less than 10, and the first-order asymptotic development is not assured to be valid. Mosser et al. (2013) proposed a semiempirical relation to convert the observed into the asymptotic spacing: $\Delta\nu_{\text{as}} = \Delta\nu_{\text{obs}}(1 + \zeta)$, with $\zeta = 0.038$ and where the reference solar values are modified to $\Delta\nu_{\odot} = 138.8 \mu\text{Hz}$ and $\nu_{\text{max},\odot} = 3104 \mu\text{Hz}$, instead of the observed values of 134.9 and 3050 μHz . The use of the second-order development leads to smaller masses and radii by 8.4% and 3.5% for RG oscillators.

The transformation of $\Delta\nu_{\text{obs}}$ into $\Delta\nu_{\text{as}}$ proposed by Mosser et al. is actually debated (Hekker et al. 2013), whereas it is generally admitted that the asteroseismic scaling relation overestimates masses. Other studies have introduced empirically calibrated corrections to the scaling laws (e.g., White et al. 2011; Miglio et al. 2012; Guggenberger et al. 2016;

Sharma et al. 2016). White et al. (2011) applies a correction on $\Delta\nu$ based on numerical models, which is a function of the effective temperature and increases it by less than 1% for an RG, and makes use of $\nu_{\text{max},\odot} = 3100 \mu\text{Hz}$ from Broomhall et al. (2009). Sharma et al. (2016) proposed a correction on $\Delta\nu$ for RGs based on stellar models, which is a function of the evolutionary stage (RGB, RC), ν_{max} , $\Delta\nu$, T_{eff} , and $[\text{Fe}/\text{H}]$. Guggenberger et al. (2016) also applies a model-based correction to the reference solar $\Delta\nu_{\odot}$ that is a function of metallicity and temperature. For most of the RGs in our sample, the modified reference $\Delta\nu_{\odot}$ using their correction yields values less than the typical 135.1 μHz . Their models also assume $\nu_{\text{max},\odot} = 3050 \mu\text{Hz}$. These three attempts tend to decrease masses and radii with respect to the original scaling relations. The Miglio et al. (2012) approach was applicable for two specific open clusters and aimed to quantify the effects of mass loss on the RGB to the horizontal branch. It is not suitable for our targets. Alternatively, some users have slightly increased the reference $\nu_{\text{max},\odot}$ to ensure that ν_{max} has been consistently measured with the same method for both the Sun and the *Kepler* stars, and this makes masses and radii decrease too. For example, Kallinger et al. (2010) and Chaplin et al. (2011) have introduced a $\nu_{\text{max},\odot}$ equal to 3120 and 3150 μHz , respectively, which has a significant influence on mass given its cubic dependence on ν_{max} . The masses drop 6.6% and 9.2%, respectively, while the radii drop 2.3% and 3.2% with respect to the Kjeldsen & Bedding (1995) reference. In our tables, we report the asteroseismic values using the corrections of Mosser et al. (2013), but we also comment on the difference with the other scaling relations (see Figure 9).

The evolutionary stage of RGs—red giant branch (RGB), main red clump (RC), secondary red clump (RC2), asymptotic giant branch (AGB)—may be deduced from the study of mixed modes measured in the power spectra (Bedding et al. 2011). When mixed modes are not detected, it is still possible to infer the nature of an RG based on $\Delta\nu$, or on mass and radii criteria (Mosser et al. 2012), or on $\Delta\nu$ and ϵ criteria (Kallinger et al. 2012). Moreover, as suggested by Beck et al. (2014), an RC or AGB identification can be discarded for a star with mass lower than $1.8 M_{\odot}$ if the separation between companions is less than $200 R_{\odot}$ along its orbit, because it corresponds to the size that a low-mass star reaches at the tip of the RGB. The engulfment of the RG's companion would occur before reaching the RC stage. This analysis was performed by Gaulme et al. (2014) for all the stars of this sample. In summary, KICs 9246715 (Rawls et al. 2016) and 8054233 are

Table 2
Orbital Parameters from Dynamical Modeling with JKTEBOP

KIC	P_{orb} (days)	T_p^a KJD	ω ($^\circ$)	e	i ($^\circ$)	$\frac{R_2}{R_1}$ (%)	$\frac{R_1 + R_2}{a}$ (%)	$\left(\frac{T_2}{T_1}\right)^4$	$\frac{L_2}{L_1}$ (%)	K_1 (km s $^{-1}$)	K_2 (km s $^{-1}$)	γ (km s $^{-1}$)
8054233	1058.16(2)	−27.69(2)	302.22(6)	0.2718(4)	89.45(1)	10.83(6)	1.924(7)	2.65(4)	3.453(5)	12.3(2)	...	−8.68(5)
4663623	358.0900(3)	129.73(2)	270.25(2)	0.43(1)	88.562(6)	18.7(3)	3.91(5)	4.0(1)	14.400(7)	23.0(7)	23(1)	−8.3(4)
9970396	235.2985(2)	142.050(2)	314(2)	0.194(7)	89.5(1)	14.05(7)	4.39(8)	2.83(4)	5.808(4)	21.4(2)	24.0(3)	−15.70(5)
7037405	207.1083(7)	87.194(9)	310.9(10)	0.238(4)	88.65(9)	12.73(6)	8.08(8)	3.79(4)	6.663(5)	23.6(2)	26.0(3)	−39.21(9)
5786154	197.9180(4)	170.865(3)	24.7(4)	0.3764(9)	88.74(3)	13.93(6)	7.14(3)	3.57(2)	7.560(4)	24.7(4)	25.7(7)	−6.3(4)
9540226	175.4439(6)	131.415(9)	4.1(4)	0.3880(2)	90 ^b	7.72(6)	7.89(2)	3.46(3)	2.110(4)	23.2(3)	31.4(5)	−12.51(9)
10001167	120.3903(5)	110.368(9)	213(2)	0.159(3)	87.5(2)	7.66(4)	11.4(2)	3.01(5)	1.849(4)	25.1(1)	25.9(8)	−103.40(6)
7377422	107.6213(4)	165.185(7)	356(1)	0.4377(5)	85.82(8)	9.15(6)	8.84(8)	2.36(7)	1.92(1)	27.5(2)	34(1)	−56.78(8)
8430105	63.32713(3)	152.7374(4)	349.3(2)	0.2564(2)	89.01(10)	10.06(2)	9.78(3)	1.716(8)	1.720(3)	27.5(2)	43.7(3)	16.29(7)
5179609	43.931080(2)	137.3016(3)	124.1(1)	0.150(1)	86.47(5)	10.57(2)	6.92(1)	2.0(4)	2.4(1)	25.0(4)	...	−21.4(2)
4569590	41.3710(1)	164.286(5)	261(4)	0.004(1)	88.6(6)	6.85(4)	21.7(1)	3.54(7)	1.615(6)	34.1(5)	51(1)	24.6(1)
5308778	40.5661(3)	137.281(5)	272(3)	0.006(5)	82.6(2)	6.02(3)	17.4(3)	0.66(2)	0.222(2)	23.8(1)	...	17.406(9)
3955867	33.65685(7)	160.104(3)	254(2)	0.019(2)	88.0(1)	11.38(5)	15.98(6)	2.79(3)	3.923(8)	37.9(2)	45(1)	14.82(4)
9291629	20.68643(4)	154.288(1)	265(2)	0.007(2)	84.10(3)	23.23(4)	23.65(5)	2.70(1)	15.10(2)	50.2(2)	51.2(5)	−30.97(5)
8702921	19.38446(2)	141.0929(7)	173(3)	0.0964(8)	86.2(3)	5.34(2)	15.6(3)	0.076(2)	0.0227(6)	14.0(3)	...	−10.28(9)
7943602	14.69199(4)	142.542(3)	103(5)	0.001(3)	81.55(7)	12.63(6)	24.40(9)	2.54(3)	3.48(2)	46.0(8)	58(3)	−185.0(1)

Notes. Systems are sorted by decreasing orbital period P_{orb} . Here, T_p stands for the time of periastron in *Kepler* Julian date, ω the argument of periastron, e the eccentricity, i the orbital plane inclination, (R_1 , T_1 , L_1) and (R_2 , T_2 , L_2) the RG and companion's radii, effective temperatures, and luminosities. The quantities K_1 , K_2 are the RV semiamplitudes, and γ is the RV offset. The least significant digit in brackets after the value indicates the uncertainty.

^a *Kepler* Julian dates KJD are related to barycentric Julian dates BJD by $\text{KJD} = \text{BJD} - 2,454,833$ days.

^b As regards 9540226, we fixed the inclination at 90° because JKTEBOP would not converge properly and its inclination is almost 90° , as the almost-vertical ingress and egress of the companion star indicate (Figure 3).

Table 3Asteroseismic Frequencies at Maximum Amplitude ν_{\max} and Observed Mean Large Spacings $\Delta\nu_{\text{obs}}$ of the Oscillating RG of Our Sample

KIC	ν_{\max} (μHz)	$\Delta\nu_{\text{obs}}$ (μHz)
4663623	54.09 ± 0.24	5.212 ± 0.019
5179609	321.84 ± 1.00	22.210 ± 0.050
5308778	48.47 ± 1.10	5.050 ± 0.050
5786154	29.75 ± 0.16	3.523 ± 0.014
7037405	21.75 ± 0.14	2.792 ± 0.012
7377422	40.10 ± 2.10	4.643 ± 0.052
8054233	46.49 ± 0.33	4.810 ± 0.015
8410637	46.00 ± 0.19	4.641 ± 0.017
8430105	76.70 ± 0.57	7.138 ± 0.031
8702921	195.57 ± 0.47	14.070 ± 0.010
9246715	106.40 ± 0.80	8.310 ± 0.020
9540226	27.07 ± 0.15	3.216 ± 0.013
9970396	63.70 ± 0.16	6.320 ± 0.010
10001167	19.90 ± 0.09	2.762 ± 0.012

Note. Systems are sorted by increasing KIC number. All ν_{\max} were obtained with DIAMONDS except for KIC 7377422, where the low signal-to-noise ratio of the oscillation spectrum prevented the routine from giving an accurate estimate. This specific ν_{\max} was fine-tuned with the help of the échelle diagram.

the only definite clump stars. KIC 8410637, which we include in our analysis, is possibly a clump star too, but its nature is unclear (Hekker et al. 2010; Gaulme et al. 2014; Brogaard et al. 2016). All of the others are RGB stars.

3. RESULTS

3.1. Nature of the Systems

From the spectroscopic measurements, all of the 17 systems we monitored exhibit spectra that are typical of stars in the RG phase. It is thus easy to track the Doppler shift of the RG spectral lines for each system. All RGs display RV modulations typical of Keplerian orbits with well-resolved amplitudes ($12\text{--}45 \text{ km s}^{-1}$) and periods that match the eclipse periods (Figures 3 and 4). Therefore, we can safely deduce that all of the RGs belong to the EB systems we suspected they belonged to, and we confirm the nature of the Gaulme et al. (2013, 2014) RG/EB candidates.

The 13 SB2s are the most interesting systems because we can determine the physical properties of each component independently from seismology. Table 4 provides the masses and radii of the RG and companion derived from the eclipse modeling described in Section 2.3. Figure 6 shows the masses, radii, and temperatures of each system’s components. In agreement with stellar evolution, we find that all companion stars are less evolved and less massive than their RG neighbors. At first glance, the companions are main-sequence K- to F-type stars. Upon closer inspection of Table 4, several of the companion stars do not exactly fall on the main sequence, either because of a larger radius than expected at a given mass and temperature (KICs 4663623, 7037405, 5786154, 9291629), or a temperature that is larger than expected (KIC 7943602). Excessive temperatures or radii could result from RG irradiation and heating by dissipation of tidal energy. The purpose of this paper is not to investigate the evolution of these binary systems, but this will be the subject of future work.

The SB1s also provide some unique astrophysical test cases. The 1,058 day orbit KIC 8054233 is composed of an RC RG

and a main-sequence F-type star on a rather eccentric orbit ($e = 0.22$). We were able to extract only three measurements of the companion’s RV, which is not enough to get a reliable estimate of its mass. We are not able to efficiently track the companion’s spectral lines because the resolution of the ARCES spectrometer does not allow us to clearly disentangle spectra with RV differences less than 10 km s^{-1} . With its long period, the RVs are separated by only 20 km s^{-1} at maximum, which makes it challenging. The three SB1s (KIC 5179609, 5308778, and 8702921) are RGs on the RGB in orbit with M dwarfs of masses M/M_{\odot} and radii R/R_{\odot} equal to $(0.6 \pm 0.01, 0.37 \pm 0.02)$, $(0.64 \pm 0.03, 0.61 \pm 0.02)$, and $(0.27 \pm 0.01, 0.28 \pm 0.01)$, respectively. The orbital eccentricities of these three systems are (0.15, 0, 0.1), and the RGs show significantly damped oscillation modes, surface activity, and spin-orbit resonances (4:1, 1:1, 5:1) (Gaulme et al. 2014). It is likely that tidal and radiative interactions have deeply affected their evolutions.

3.2. Mode Suppression in Short-period Systems Is Real

Gaulme et al. (2014) analyzed the light curves of these systems and concluded that the four with no detectable RG oscillations were indeed RG/EBs. These are four of the six shortest-period binaries in the sample (see Tables 2 and 4). Without any spectra to confirm this, one of their arguments was that the modeled ratio of radii $R_{\text{cmp}}/R_{\text{RG}}$ was less than 0.15. Such a small ratio permits basically two scenarios: a nonoscillating RG with a main-sequence companion, or an exoplanet and a main-sequence star whose pulsations could not be measured in long-cadence data. However, in the case of an exoplanet, none or very shallow secondary eclipses would be observable, while all four of these systems display clear secondary eclipses.

The lack of detectable modes of the RG component can also potentially be explained if it is a younger, less massive star with a ν_{\max} larger than the $283 \mu\text{Hz}$ Nyquist frequency of long-cadence data. To test this scenario, we apply the inverse asteroseismic scaling relations of Mosser et al. (2013) to the masses and radii derived from dynamical models (Table 4) to estimate ν_{\max} , fully aware that the scaling relations, whose accuracy we are testing in this study, can potentially give erroneous results. Nonetheless, we find that the four RGs have expected ν_{\max} values well below the Nyquist frequency. More precisely, KICs 4569590, 3955867, 9291629, and 7943602 would display ν_{\max} of 27 ± 1 , 59 ± 4 , 61 ± 2 , and $74 \pm 4 \mu\text{Hz}$, respectively.

We therefore confirm that oscillations of RGs in close EBs—that is, with $(R_{\text{RG}} + R_{\text{cmp}})/a \geq 0.16$ —can be suppressed enough to be undetectable. We stress that here we measure suppression of the entire mode envelope, not the suppression of only $\ell = 1$ modes due to internal magnetic fields (Fuller et al. 2015; Stello et al. 2016). The reasons for this suppression need further investigation.

3.3. Asteroseismic Scaling Relations Overestimate Mass and Radius

In what follows, we assume that the detailed dynamical modeling gives an accurate representation of the stellar parameters in which we are interested and which we can use to compare to seismic inferences. Figure 7 shows the departure of M/M_{\odot} , R/R_{\odot} , $\log g$, and $\bar{\rho}/\bar{\rho}_{\odot}$ from asteroseismic scaling

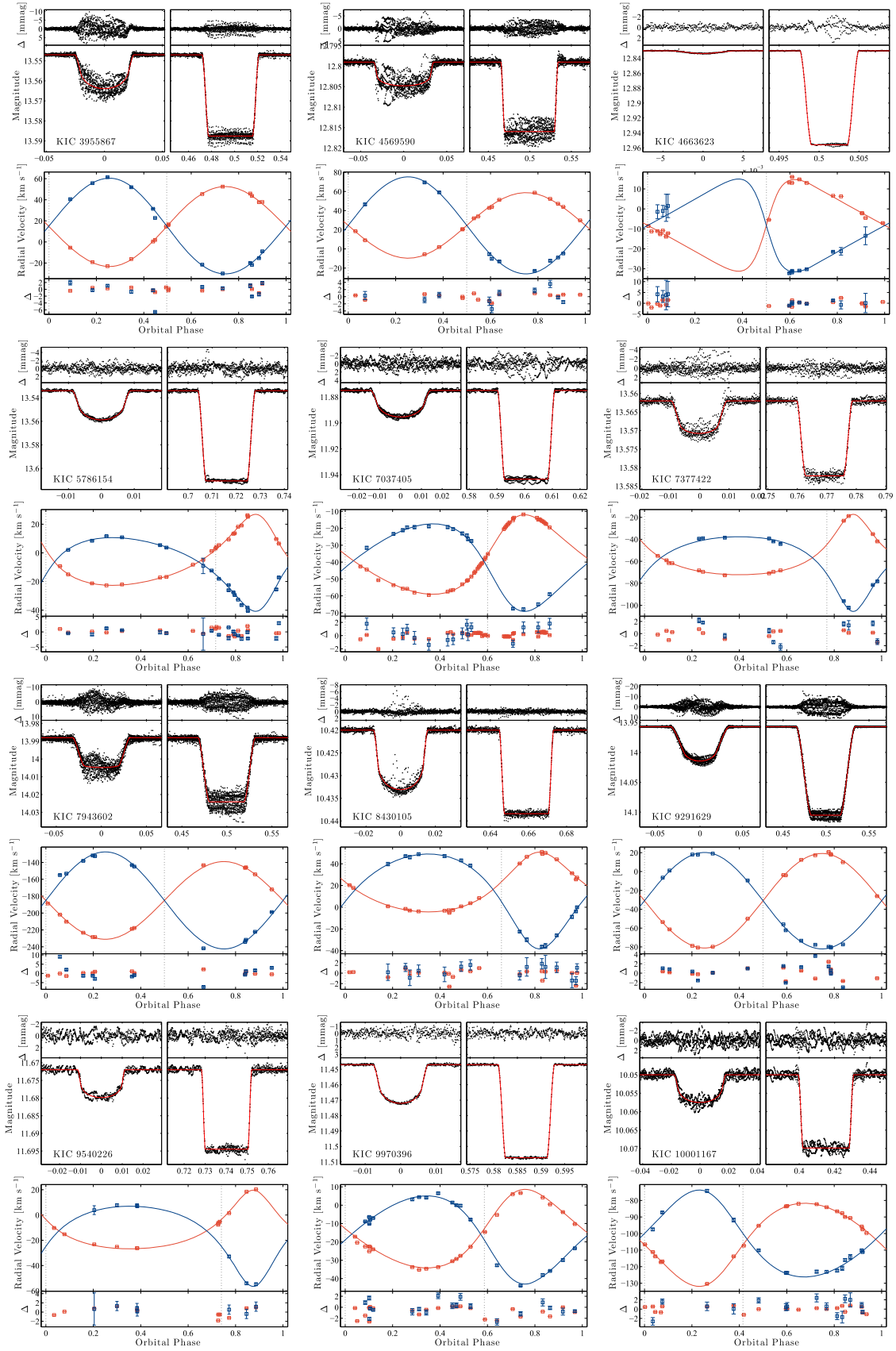


Figure 3. Combined modeling of *Kepler* light curves and RV measurements. All SB2 systems are represented here, except for KIC 9246715, which can be found in Rawls et al. (2016).

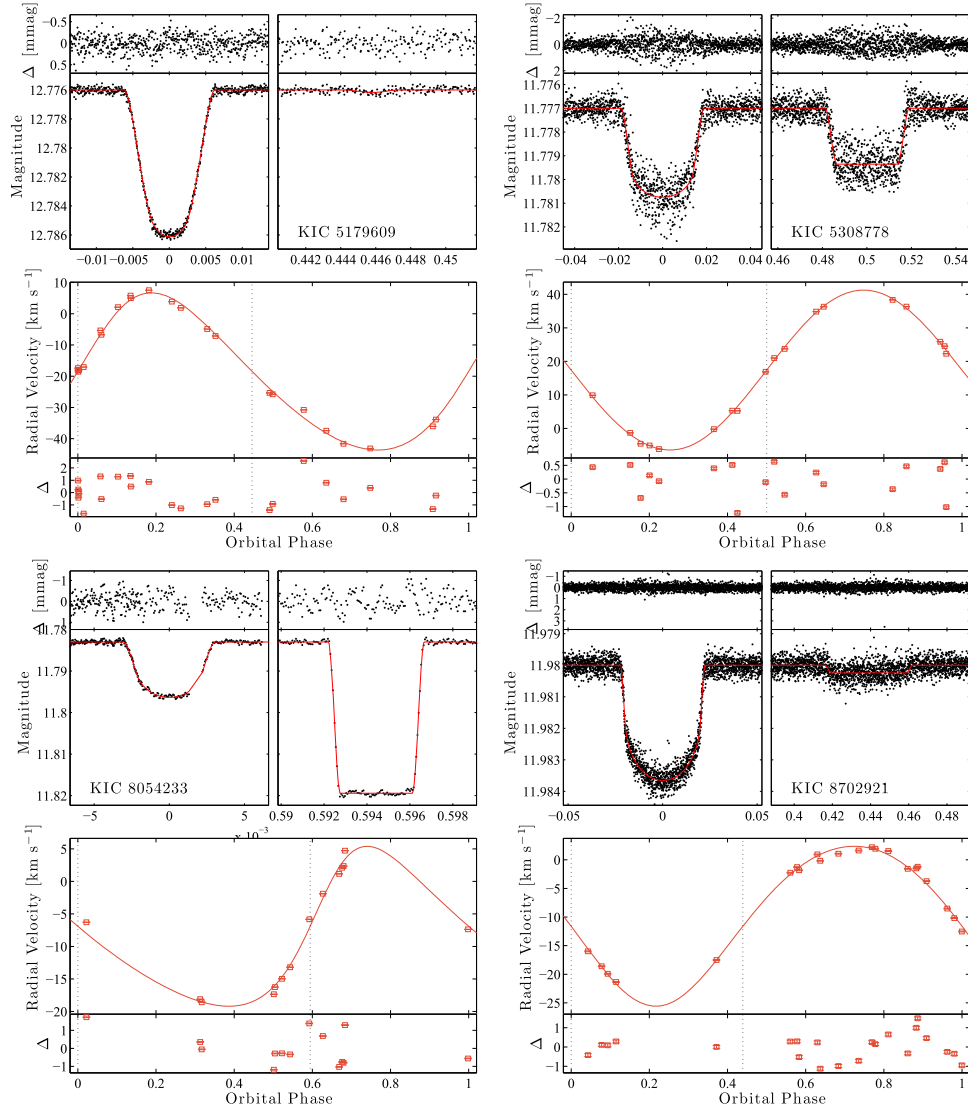


Figure 4. Combined modeling of *Kepler* light curves and RV measurements. All SB1 systems are represented here.

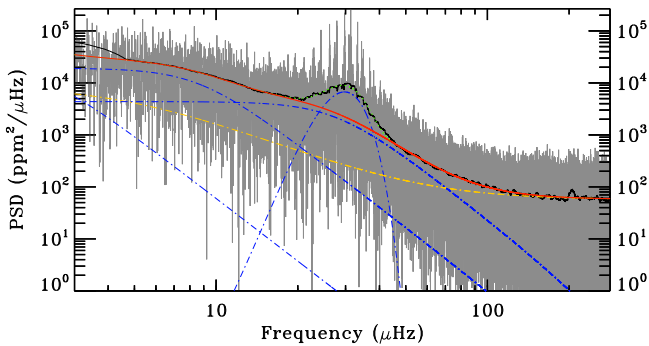


Figure 5. Background fit of KIC 5786154, as derived by DIAMONDS. The original PSD is shown in gray, while a smoothed version with boxcar width set to $5 \Delta\nu$ is shown as a black line to guide the eye. The red thick line represents the background model without the Gaussian envelope, while the green dotted line accounts for the additional Gaussian component. The individual components of granulation and long-trend variation are shown by blue dot-dashed lines. The yellow dot-dashed line shows the superposition of white and colored noise.

relations with respect to the dynamical models of the 10 SB2 systems with a pulsating RG component. The effective temperatures used as input in the scaling relations are those derived from the visible spectra (Table 1). We also include the estimated parameters of KICs 8410637 and 9246715 from Frandsen et al. (2013) and Rawls et al. (2016).

A clear overestimation by seismic scaling is observed for masses and radii for most systems in Figures 7 and 8. On average, the scaling relation corrections of Mosser et al. (2013) provide masses and radii larger by $15.4\% \pm 10.9\%$ and $5.1\% \pm 3.0\%$, respectively, while mismatches can reach about 35% and 11% (Table 4). The “standard” scaling relations lead to overestimation of masses and radii by $25.9 \pm 11.9\%$ and $8.8\% \pm 3.1\%$ when using $\nu_{\max,\odot} = 3050 \mu\text{Hz}$ (Kjeldsen & Bedding 1995), $17.6\% \pm 11.2\%$ and $6.3\% \pm 3.0\%$ with $\nu_{\max,\odot} = 3120 \mu\text{Hz}$ (Kallinger et al. 2010), and $14.3\% \pm 10.8\%$ and $5.4\% \pm 3.0\%$ with $\nu_{\max,\odot} = 3150 \mu\text{Hz}$ (Chaplin et al. 2011). The temperature-dependent correction of $\Delta\nu$ by White et al. (2011) leads to masses and radii larger by

Table 4
Stellar Physical Parameters from Dynamical Modeling (Subscripts “rv”) and Asteroseismic Scaling Relations (Subscripts “ast”)

KIC	Red Giant									Companion			d (kpc)
	M_{rv} (M_{\odot})	M_{ast} (M_{\odot})	R_{rv} (R_{\odot})	R_{ast} (R_{\odot})	$\log g_{\text{rv}}$ (dex)	$\log g_{\text{ast}}$ (dex)	$\bar{\rho}_{\text{rv}}$ ($10^{-3}\rho_{\odot}$)	$\bar{\rho}_{\text{ast}}$ [$10^{-3}\rho_{\odot}$]	T_{eff} (K)	M [M_{\odot}]	R (R_{\odot})	T_{eff} (K)	
Double-line Spectroscopic Binaries (SB2)													
8410637 [†]	1.56(3)	1.70(7)	10.7(1)	11.2(2)	2.57(1)	2.569(5)	1.26(6)	1.205(9)	4800(100)	1.32(2)	1.57(3)	6490(160)	0.87
4663623	1.36(9)	1.74(7)	9.7(2)	10.5(1)	2.60(2)	2.640(5)	1.48(6)	1.52(1)	4812(92)	1.34(7)	1.82(6)	6808(140)	1.92
9970396	1.14(3)	1.36(4)	8.0(2)	8.47(7)	2.69(2)	2.716(3)	2.2(1)	2.234(7)	4916(68)	1.02(2)	1.12(2)	6378(91)	0.92
7037405	1.25(4)	1.25(4)	14.1(2)	14.2(2)	2.24(1)	2.230(3)	0.45(1)	0.436(4)	4516(36)	1.14(2)	1.80(2)	6303(53)	1.43
5786154	1.06(6)	1.36(6)	11.4(2)	12.5(2)	2.35(2)	2.377(5)	0.71(2)	0.694(6)	4747(100)	1.02(4)	1.59(3)	6527(138)	2.82
9540226	1.33(5)	1.45(5)	12.8(1)	13.6(2)	2.349(8)	2.334(4)	0.639(8)	0.578(5)	4692(65)	0.98(3)	0.99(1)	6399(90)	1.29
9246715 [†]	2.149(7)	2.19(6)	8.30(4)	8.28(8)	2.932(4)	2.943(4)	3.76(5)	3.86(2)	5030(45)	2.171(7)	8.37(5)	4990(90)	0.39
10001167	0.81(5)	1.06(4)	12.7(3)	13.6(2)	2.14(2)	2.200(4)	0.39(2)	0.427(4)	4700(66)	0.79(3)	0.98(2)	6191(91)	0.69
7377422	1.05(8)	1.2(2)	9.5(2)	9.9(6)	2.50(2)	2.52(2)	1.21(4)	1.21(3)	4938(110)	0.85(3)	0.87(2)	6120(143)	2.59
8430105	1.31(2)	1.52(6)	7.65(5)	8.1(1)	2.788(4)	2.802(4)	2.93(3)	2.85(3)	5042(68)	0.83(1)	0.770(5)	5771(78)	0.61
4569590	1.56(10)	...	14.1(2)	...	2.33(1)	...	0.56(1)	...	4706(152)	1.05(4)	0.96(2)	6456(211)	2.37
3955867	1.10(6)	...	7.9(1)	...	2.68(1)	...	2.19(4)	...	4884(83)	0.92(3)	0.90(1)	6312(108)	2.19
9291629	1.14(3)	...	7.99(5)	...	2.691(5)	...	2.24(2)	...	4713(151)	1.12(2)	1.86(1)	6041(194)	2.28
7943602	1.0(1)	...	6.6(2)	...	2.79(2)	...	3.40(9)	...	5096(100)	0.78(5)	0.83(2)	6431(128)	2.68
Single-line Spectroscopic Binaries (SB1)													
8054233	...	1.60(6)	...	10.7(1)	...	2.581(5)	...	1.294(8)	4971(90)	1.10(4)	1.16(2)	6344(117)	1.61
5179609	...	1.18(3)	...	3.50(3)	...	3.423(3)	...	27.6(1)	5003(54)	0.60(1)	0.370(3)	5950(304)	0.88
5308778	...	1.5(1)	...	10.1(3)	...	2.60(1)	...	1.43(3)	4900(44)	0.64(3)	0.61(2)	4416(52)	1.47
8702921	...	1.67(5)	...	5.32(5)	...	3.209(4)	...	11.07(2)	5058(86)	0.274(9)	0.284(3)	2654(49)	0.97

Note. The parameters M , R , $\log g$, and $\bar{\rho}$ refer to stellar masses, radii, surface gravities, and mean densities, T_{eff} effective temperatures, and d system distances. Systems are sorted by decreasing orbital period. The dagger symbols [†] indicate that the dynamical values of KICs 8410637 and 9246715 are taken from Frandsen et al. (2013) and Rawls et al. (2016), respectively. For SB1 systems, the parameters of the companion stars are deduced by combining asteroseismic masses and radii of the RG with the mass function obtained from light curve and radial velocity modeling.

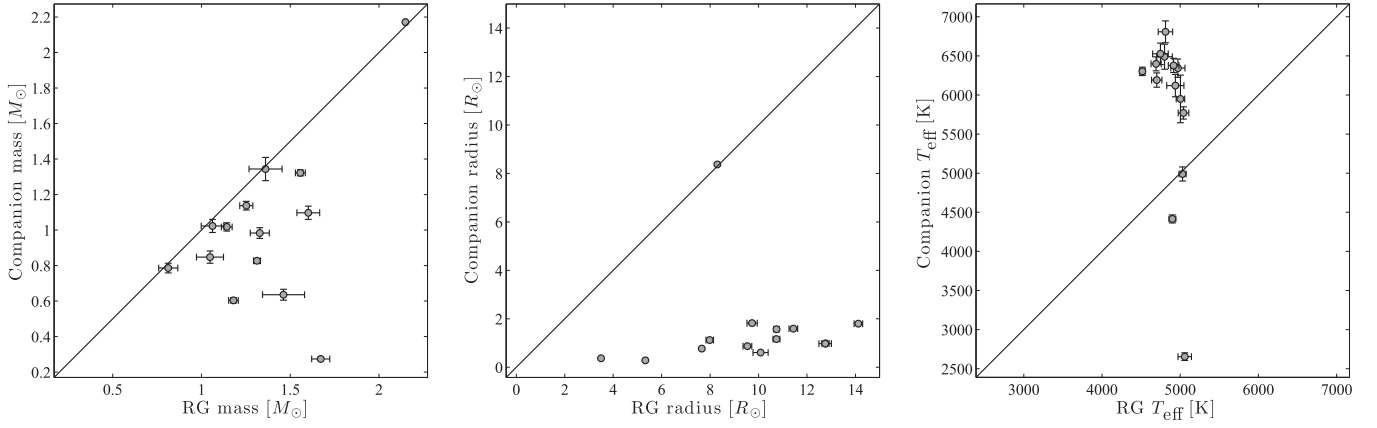


Figure 6. Red giant vs. companion physical parameters. For SB1s, the masses and radii of the companion stars were obtained by combining asteroseismic masses and radii with the dynamical mass function (Equation (5)).

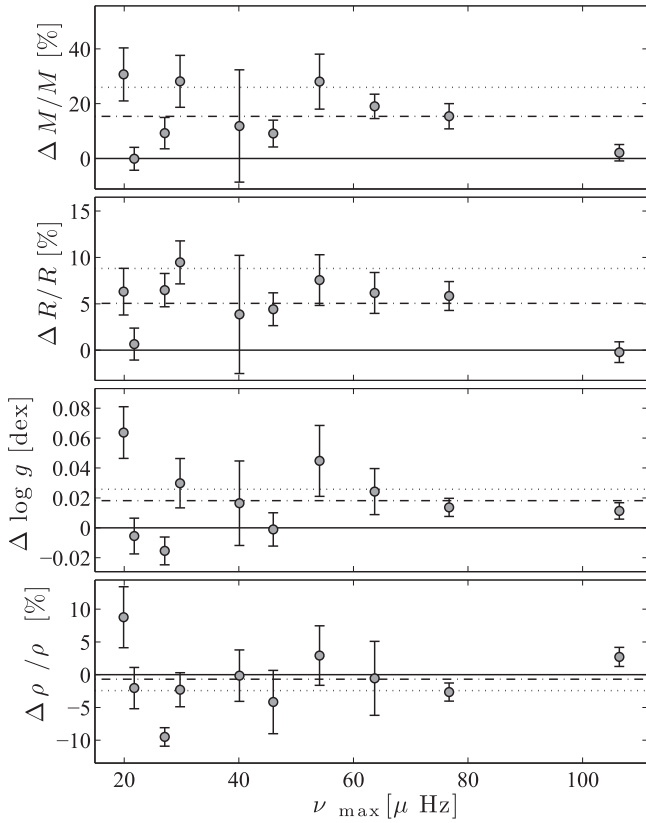


Figure 7. Dynamical modeling vs. asteroseismic scaling relations, in the sense of (seismo-RV)/RV, as a function of ν_{\max} . The asteroseismic values are obtained with the Mosser et al. (2013) scaling. The dot-dashed lines indicate the average levels in each panel, and the dotted lines the averages obtained with the “standard” scalings, including ν_{\max} and $\Delta\nu$ from Kjeldsen & Bedding (1995).

13.4% and 4.1% on average. Regarding the study of Sharma et al. (2016), adopting their correction on $\Delta\nu$ provides masses and radii that are overestimated by 13.5% and 4.0%, respectively. Guggenberger et al. (2016), who worked with the $\nu_{\max,\odot}$ from Kjeldsen & Bedding (1995) for their models, are relatively off with respect to the other corrections. However, if we make use of the $\nu_{\max,\odot}$ from Chaplin et al.

(2011) in their scaling relations, the output is very similar to the others. Figure 9 summarizes these comparisons for each system.

Since both of these quantities (mass and radius) are larger than the dynamical quantities, the discrepancy in surface gravity and mean density (ratios of the two) is not as severe. We measure $\log g$ larger by 0.017 ± 0.023 dex and 0.025 ± 0.023 dex with Mosser and standard scaling relations, whereas densities are lower by $-0.8\% \pm 4.8\%$ and $-2.5\% \pm 4.7\%$, respectively. There is no clear trend with ν_{\max} , and the only obvious clump star—the double-RG system KIC 9246715—shows agreement between the measurements.

4. DISCUSSION

The key finding in this study is that asteroseismic masses and radii for a sample of RGs are systematically larger than those obtained through detailed binary modeling. Huber et al. (2012) used interferometry of pulsating stars to derive radii and compare to seismic values. While they found a scatter for their four RGs similar to what we find, the radii were not systematically larger. Frandsen et al. (2013) were the first to test the asteroseismic scaling relations with an eclipsing RG star, KIC 8410637. In that analysis, the asteroseismic mass and radius were indeed larger than the dynamical ones, and the uncertainties were large enough that the comparison was statistically consistent. Brogaard et al. (2016) have extended that analysis to another eclipsing RG, KIC 9540226 (which we also study), and reach the same conclusion. In our study here, the various shades of the asteroseismic scaling relations we tested lead to similar results. The outliers are those obtained with solar reference values from Kjeldsen & Bedding (1995), regardless of the evolutionary stage, and corrections from Sharma et al. (2016) for the two RC giants. The largest influence on the output from the scaling relations is the choice of $\nu_{\max,\odot}$. With a sample composed of 10 stars—mostly RGBs—masses are overestimated by about 15% and radii by 5%.

It is important to first understand if there is something specific to these particular stars, that is, RGs in binary systems, that could be causing the inconsistencies in these results. The obvious factor here is the potential influence of binarity. On one hand, tidal influences on the pulsations could lead to poor measurements of $\Delta\nu$ or ν_{\max} . Indeed, as discussed earlier, four

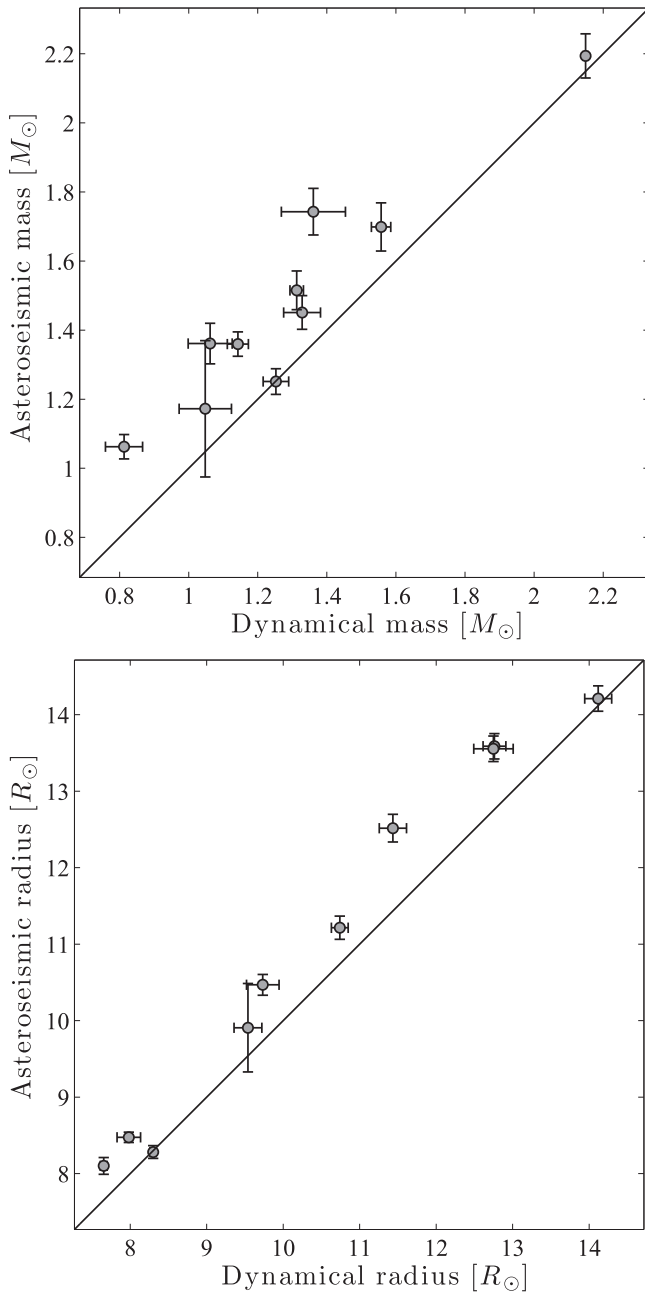


Figure 8. Masses and radii from asteroseismic scaling relations from Mosser et al. (2013) vs. those obtained from dynamical modeling.

RGs in short periods have undetectable modes—a fraction much larger than one would expect. These happen to be in short-period orbits. Others have lower pulsation amplitudes than expected. On the other hand, tides could also distort the shape of the stars, leading to models that provide inaccurate radii or other orbital parameters. Any such scenarios should show a trend in the mass and radius disagreement with orbital period; however, the results in Figure 10 (top panel) do not support this. Even the longest-period systems have some of the largest mismatches in mass and radius. Thus, even if binarity does significantly suppress mode amplitudes, the frequency information appears to be largely unaffected (but with a loss of

precision). Furthermore, most of the systems do not show appreciable phase effects (e.g., ellipsoidal variations) out of eclipse in the time series, and moreover, such effects would not alter the mass estimation, which is mainly obtained from the RV data. As these are detached systems, we do not consider the effects of mass transfer between stars. Note that there is no dependence of the mass or radius overestimation as a function of T_{eff} or $[\text{Fe}/\text{H}]$ (Figure 10).

Another potential culprit in the scaling relations is the effective temperature. Overestimated temperatures can indeed lead to larger values of mass and radius from the scaling laws even though the functional dependence on T_{eff} is rather weak (to the $3/2$ and $1/2$ power for mass and radius, respectively). The temperatures we use are derived from visible spectra that do contain the flux from the companion star, although the companions are relatively faint. Figure 2 shows that the visible temperatures we use in the scaling relations are often larger than the APOGEE-derived ones. Their median difference is 101 K. Decreasing the temperatures artificially by 100 K shifts the asteroseismic masses lower by 3.1% and radii by 1.0%, which does not change our conclusions.

The other quantities, ν_{max} and $\Delta\nu$, are almost always straightforward to measure and have rather small uncertainties. Figure 8 shows a scatter plot of the seismic and binary masses and radii. In a few cases, the large errors on the seismic quantities are due to suppressed modes, making ν_{max} more difficult to measure precisely. Still, the systematic remains. Furthermore, we find that the spectroscopic gravity is consistently larger than the seismic gravity, which has also been observed in the large APOKASC survey (e.g., Pinsonneault et al. 2014; Holtzman et al. 2015). Figure 11 shows that this is also the case when compared to the surface gravities obtained from the light-curve modeling masses and radii.

If we exclude KIC 10001167 in Figure 7, which has the lowest ν_{max} and metallicity, the asteroseismic density is systematically underestimated. Since the density relies exclusively on the $\Delta\nu$ measurement, this suggests that not using the universal pattern and measuring the individual frequencies could perhaps yield a different large separation.

One of the most important consequences of these results is that mass overestimation leads to age underestimation. Figure 12 shows this quantitatively for a theoretical collection of stars. Consider RGs whose masses are determined asteroseismically (along the y axis). For that given mass, the x axis is the amount the mass might potentially be overestimated, and the gray scale exhibits the difference in age between stars of higher and lower mass on the RGB. The data were obtained from BaSTI (“standard scaled solar”) isochrones (Pietrinferni et al. 2004). Also plotted are eight of the stars from our sample whose mass is overestimated by at least $0.1 M_{\odot}$. While this is just an approximate demonstration since we fix the metallicity of the isochrones and do not take into account uncertainties on the masses, for example, it does illustrate the significant errors one could make in determining the age of RGs, particularly for inherently low-mass stars. For example, seismology would predict KIC 10001167 to be over 12 billion years younger than it would be if its mass were what is determined through binary modeling. More metal-rich

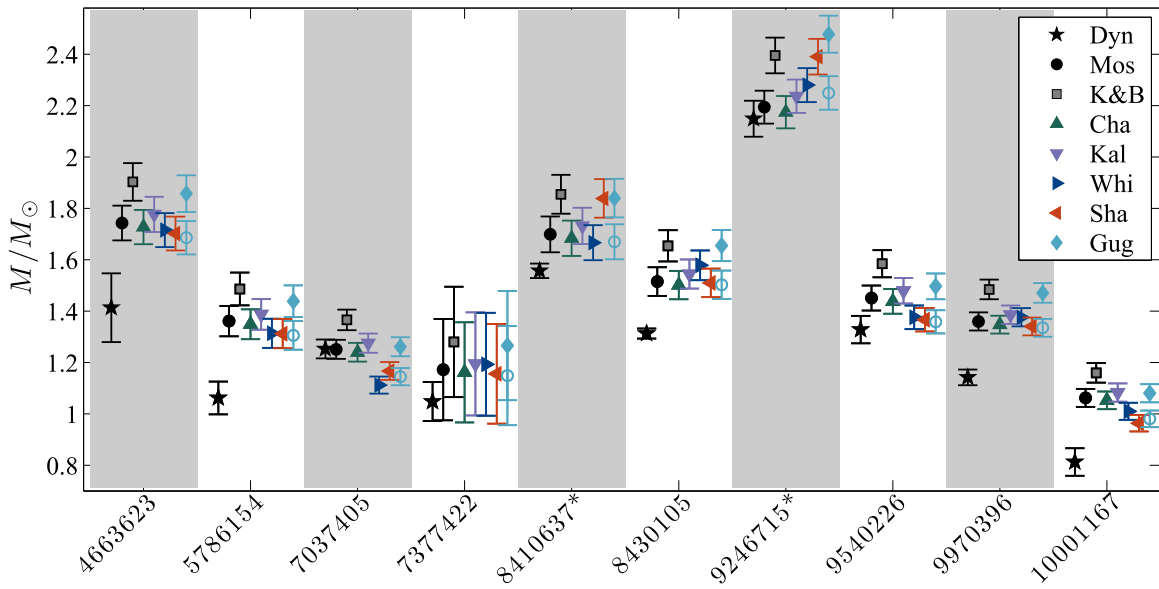


Figure 9. Mass estimates from dynamical modeling (“Dyn”) and seven asteroseismic scaling relations. The abbreviation “Mos” stands for Mosser et al. (2013), “K&B” Kjeldsen & Bedding (1995), “Cha” Chaplin et al. (2011), “Kal” Kallinger et al. (2010), “Whi” White et al. (2011), “Sha” Sharma et al. (2016), and “Gug” Guggenberger et al. (2016). For Guggenberger et al. (2016), the diamonds indicate the result with $\nu_{\max,\odot} = 3050 \mu\text{Hz}$ and circles with $\nu_{\max,\odot} = 3150 \mu\text{Hz}$. The asterisks next to the KIC numbers indicate the two likely red clump red giants. A similar trend is observed for radii.

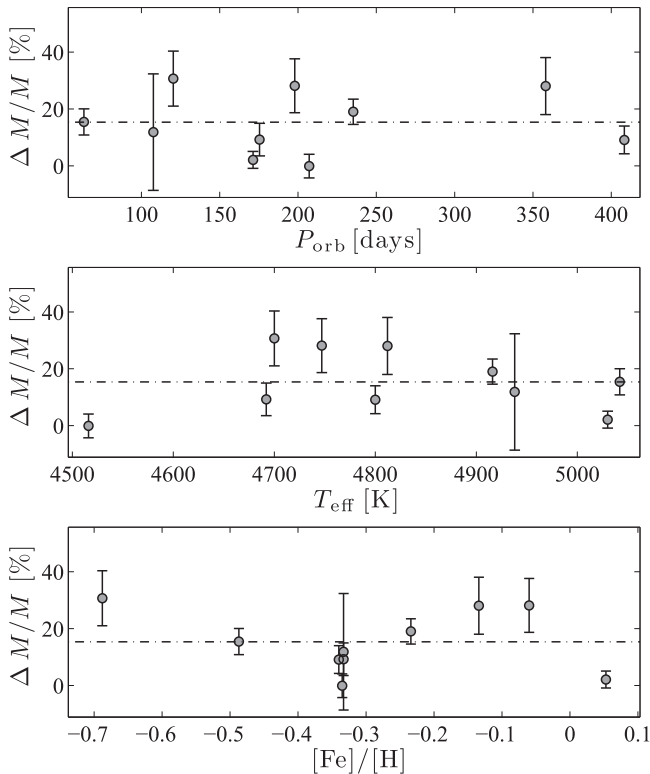


Figure 10. Dynamical modeling vs. asteroseismic scaling relations, in the sense of (seismo-RV)/RV, as a function of P_{orb} , T_{eff} , and $[\text{Fe}/\text{H}]$. The asteroseismic values are obtained with the scaling from Mosser et al. (2013). The dot-dashed lines indicate the average levels in each panel.

isochrones would increase the age overestimation, while more metal-poor ones would decrease it.

If this is a systematic effect for all pulsating RGs, it could have consequences for other current work. For example, the recently discovered α -enhanced RGs (Chiappini et al. 2015; Martig et al. 2015), which appear young because of their rather

large (seismic) masses, could indeed be less massive with ages that are more in line with other α -enhanced stars.¹¹ The interpretation of large galaxy surveys using asteroseismic data in the context of galaxy population modeling is also an area where these results could be important. For example, Sharma et al. (2016) concluded that the galaxy population model overpredicts the number of low-mass stars when compared to seismic inferences of RGs. An alternative interpretation given our findings is that seismology may be overpredicting the number of high-mass stars.

5. CONCLUSIONS

We have identified and studied a key set of RG stars in eclipsing binaries that allow for independent methods to obtain masses and radii. By choosing the masses and radii obtained from the binary modeling as the ground truth, we find that (all) seismic scaling relations overestimate both quantities.

Our measurements will be of tremendous use in detailed modeling of these RGs that may yield insights into how the scaling laws break down away from the asymptotic limit. In any case, a sense of caution is needed when applying the scaling laws to large samples of giants if, for example, a high accuracy on ages is needed. Even though it may be likely that a simple empirical recalibration of the scaling laws for evolved stars can be applied, as many recent studies have attempted, a more satisfactory understanding is certainly desired.

It is also critical to increase the sample size. We have recently found 16 more RG/EB candidates (Gaulme et al., in preparation), which will be promising systems to verify the findings in this work. Among those 16, 10 display oscillations, of which six are SB2s. We have started monitoring their RVs in early 2016, both with the échelle spectrographs ARCES at

¹¹ There are other reasons to believe these stars are indeed young, however, such as their location in the galaxy.

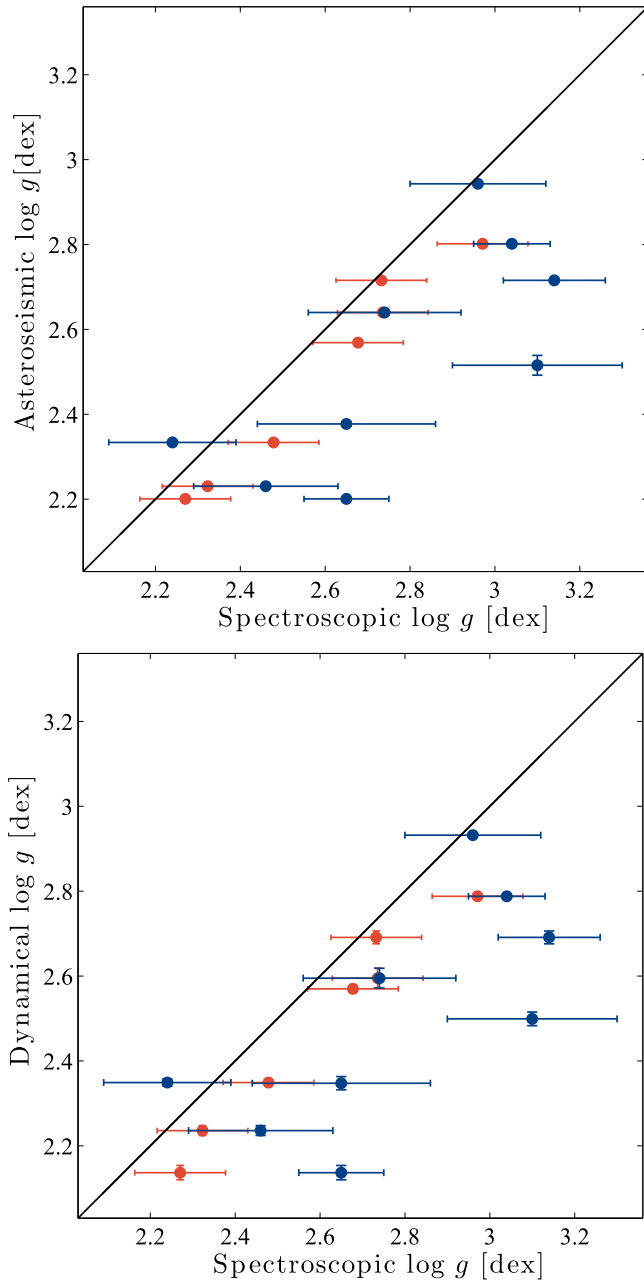


Figure 11. Surface gravity $\log g$ from asteroseismic scaling relations from Mosser et al. (2013) vs. spectrometric estimates with ARCES and APOGEE. Blue symbols indicate the visible ARCES values, and red symbols the IR APOGEE values.

APO and HERMES of the Mercator telescope at La Palma Observatory.

The authors thank P. Beck, S. Hasselquist, D. Stello, S. Frandsen, M. Pinsonneault, and K. Belkacem. J.J. and P.G. acknowledge support from NASA ADAP grant NNX14AR85G. E.C. is funded by the European Community's Seventh Framework Programme (FP7/2007–2013) under grant agreement N°312844 (SPACEINN). C.F.B. and S.M. acknowledge support from NSF grant AST-1517592. Most of this paper

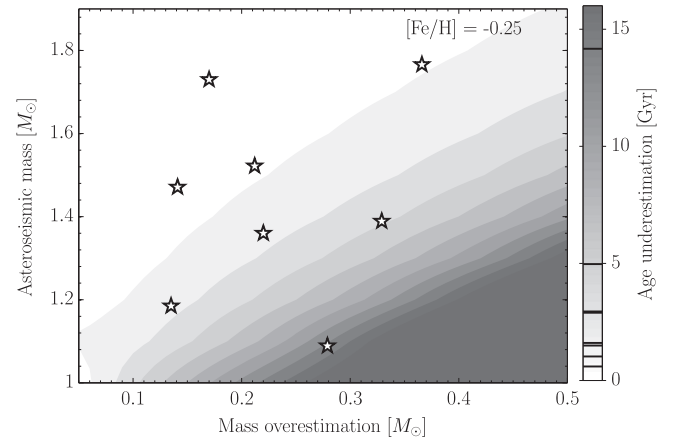


Figure 12. Stellar age overestimation from mass overestimation using isochrones. The y axis denotes stellar mass measured from seismic scaling relations, and the x axis depicts how much larger than the true mass this is. The gray scale indicates the difference in age on the RGB that stellar models would predict for those two initial masses. Also plotted are eight of the stars in this study that have the largest mass discrepancy between seismology and binary modeling. The anticipated age differences for those stars are also indicated on the color bar with horizontal lines. The gray scale is clipped at 14 Gyr. The metallicity of the isochrones is indicated. The isochrones were obtained from the BaSTI database (Pietrinferni et al. 2004).

is based on observations obtained with the Apache Point Observatory 3.5 m telescope, which is owned and operated by the Astrophysical Research Consortium. Funding for SDSS-III has been provided by the Alfred P. Sloan Foundation, the Participating Institutions, the National Science Foundation, and the U.S. Department of Energy Office of Science. The SDSS-III web site is <http://www.sdss3.org/>. SDSS-III is managed by the Astrophysical Research Consortium for the Participating Institutions of the SDSS-III Collaboration including the University of Arizona, the Brazilian Participation Group, Brookhaven National Laboratory, Carnegie Mellon University, University of Florida, the French Participation Group, the German Participation Group, Harvard University, the Instituto de Astrofísica de Canarias, the Michigan State/Notre Dame/JINA Participation Group, Johns Hopkins University, Lawrence Berkeley National Laboratory, Max Planck Institute for Astrophysics, Max Planck Institute for Extraterrestrial Physics, New Mexico State University, New York University, Ohio State University, Pennsylvania State University, University of Portsmouth, Princeton University, the Spanish Participation Group, University of Tokyo, University of Utah, Vanderbilt University, University of Virginia, University of Washington, and Yale University.

Software: JKTLD: <http://www.astro.keele.ac.uk/jkt/codes/jktld.html>.

APPENDIX

Table 5 displays the complete set of radial velocities we took for this work. This obviously excludes the measurements for KIC 8410637 and 9246715, which are provided in Frandsen et al. (2013) and Rawls et al. (2016), respectively.

Table 5
Radial Velocities (Part I)

Date KJD	RV1 (km s ⁻¹)	RV2 (km s ⁻¹)
KIC 3955867		
1704.7441	-16.20(5)	51.9(5)
1741.7754	1.85(5)	22.7(2)
1766.5527	-19.15(5)	55.8(3)
1936.9669	-22.96(5)	61.4(3)
1958.9400	37.85(6)	-8.9(5)
1990.8794	45.86(5)	-19.9(6)
2032.6426	-5.46(5)	40.5(7)
2111.7190	0.43(5)	31.4(4)
2113.5592	14.49(5)	...
2121.6013	52.47(4)	-29.9(4)
2125.7532	43.68(5)	-21.7(2)
2126.7446	37.69(5)	-15.4(5)
2286.9775	45.42(5)	-21.6(3)
2315.8251	15.98(4)	...
2315.8500	16.67(4)	...
KIC 4569590		
1741.7931	43.87(7)	-10(1)
1936.9265	-5.57(7)	69.4(8)
1958.8371	52.25(8)	-12(1)
1967.9110	9.08(7)	47(1)
1980.8471	1.97(6)	59.0(8)
2032.7087	51.27(6)	-13.0(7)
2069.6493	31.99(6)	...
2111.7513	33.93(7)	...
2113.7085	42.82(6)	-5(1)
2121.6195	58.69(6)	-22.9(7)
2125.6981	47.16(6)	-8.9(4)
2126.6056	43.86(6)	-4.7(4)
2129.5493	29.78(7)	...
2315.8739	20.64(7)	...
2315.8975	20.38(7)	...
2462.6855	18.50(7)	...
KIC 4663623		
1737.7064	-7.11(2)	...
1741.6719	-8.52(2)	...
1958.8201	16.01(2)	-31.0(3)
1980.8653	12.99(2)	-30.2(3)
2032.6816	6.25(2)	-21(2)
2069.6872	-4.53(2)	-13(4)
2113.6769	-11.13(4)	-1(4)
2121.7263	-10.87(5)	-1(3)
2126.6409	-13.93(2)	1(7)
2462.6391	-11.27(2)	...
2475.7933	-12.71(2)	...
2487.5708	-12.22(3)	1(6)
2639.9061	-5.46(2)	...
2670.8693	13.17(2)	-32.2(3)
2674.8132	13.00(2)	-31.8(3)
2685.9605	14.79(2)	-30.9(3)
2736.8396	6.57(2)	-21.5(3)
2780.6121	-2.25(3)	...
2780.6286	-2.13(2)	...
KIC 5179609		
1257.8837	-30.77(3)	...
1272.7406	-33.86(3)	...
1341.9043	-25.34(3)	...
1569.8694	-41.63(3)	...
1591.9183	7.53(3)	...

Table 5
(Continued)

Date KJD	RV1 (km s ⁻¹)	RV2 (km s ⁻¹)
1611.8624	-37.44(3)	...
1704.6737	-43.11(3)	...
1711.7021	-36.07(3)	...
1737.6376	-25.79(4)	...
1765.5876	5.79(3)	...
1765.6280	5.01(3)	...
1939.9000	2.11(3)	...
1990.8967	1.88(3)	...
2069.7258	-5.34(3)	...
2111.7697	-17.07(3)	...
2113.7604	-6.73(3)	...
2121.6748	3.89(3)	...
2125.6580	-4.89(3)	...
2126.5887	-7.13(3)	...
2286.9007	-18.59(3)	...
2286.9223	-17.95(3)	...
2462.5796	-17.41(3)	...
2462.5988	-18.06(3)	...
2506.5914	-18.11(3)	...
KIC 5308778		
1569.9394	38.33(4)	...
1591.9508	-0.21(4)	...
1611.9306	36.32(4)	...
1623.8267	-1.31(4)	...
1683.6971	34.83(4)	...
1737.5909	24.54(4)	...
1737.7662	22.29(4)	...
1741.6243	9.89(4)	...
1765.6147	36.30(4)	...
1939.9725	25.86(4)	...
1958.9553	5.30(4)	...
1990.9345	-5.07(4)	...
2111.7005	-4.58(4)	...
2113.6109	-6.16(4)	...
2121.7445	5.25(4)	...
2125.5745	20.99(4)	...
2126.6561	23.74(4)	...
2286.9375	16.88(4)	...
KIC 5786154		
1272.7870	-17.16(2)	...
1340.8309	19.10(2)	...
1569.8874	6.49(2)	-17.1(4)
1591.9356	-15.03(2)	2.05(5)
1611.8805	-21.27(2)	8.5(5)
1623.8985	-22.68(2)	11.7(3)
1704.6241	-4.94(2)	...
1711.6255	1.25(2)	-12.3(2)
1741.5950	26.26(2)	-38.2(3)
1765.6455	9.62(2)	...
1939.8774	25.15(2)	-40.6(3)
1980.9316	-9.30(2)	...
2032.7296	-22.03(2)	10.9(1)
2069.7759	-16.79(2)	...
2111.5711	4.26(2)	...
2113.5789	5.45(2)	-18.1(2)
2121.7081	9.31(2)	-22.5(1)
2125.6755	13.28(2)	-27.5(3)
2126.7248	13.64(2)	-29.4(3)
2129.5945	18.22(2)	-32.6(1)
2487.7330	-8.26(2)	...
2506.5403	3.05(3)	...

Table 5
(Continued)

Date KJD	RV1 (km s ⁻¹)	RV2 (km s ⁻¹)
KIC 7037405		
1623.9163	-44.44(4)	-31.5(9)
1724.7334	-40.6(1)	...
1726.7233	-38.4(1)	...
1727.7210	-37.4(1)	...
1751.6322	-14.3(1)	...
1752.6307	-13.7(1)	...
1924.8930	-46.4(1)	...
1925.9023	-45.6(1)	...
1927.9058	-43.9(1)	...
1928.8729	-42.9(1)	...
1929.8687	-42.1(1)	...
1930.8812	-41.1(1)	...
1936.9120	-35.26(3)	...
1950.8357	-20.5(1)	...
1951.8220	-19.7(1)	...
1952.8254	-18.8(1)	...
1953.7985	-18.0(1)	...
1954.8094	-17.3(1)	...
1955.8431	-16.5(1)	...
1958.7673	-15.22(4)	-67.6(5)
1967.9409	-11.77(3)	-67.9(8)
1979.7451	-13.7(1)	...
1980.8136	-14.84(3)	-65.0(8)
1981.7555	-14.6(1)	...
1982.7855	-14.9(1)	...
1983.7663	-15.5(1)	...
1984.7620	-15.9(1)	...
1985.7646	-16.3(1)	...
1986.7622	-17.0(1)	...
1987.7560	-17.4(1)	...
1990.8100	-19.47(3)	-59.1(8)
2032.6241	-42.64(3)	...
2069.6345	-55.72(3)	-21.1(9)
2111.5547	-56.78(3)	...
2113.5972	-56.50(3)	-20.5(8)
2121.5857	-53.13(3)	-23.1(8)
2125.6083	-51.09(3)	-24.2(8)
2126.6259	-50.67(3)	-26.4(9)
2129.5633	-48.59(3)	-27.5(6)
2286.9600	-58.05(3)	-19.3(10)
2315.9580	-57.50(3)	-19.3(9)
2462.5620	-50.71(5)	...
2475.7807	-53.66(3)	-23.3(7)
2487.6314	-55.83(3)	-19.4(8)
2506.6085	-59.54(3)	-18.8(8)
KIC 7377422		
1697.7442	-61.74(4)	...
1711.7231	-69.59(3)	-39.0(2)
1741.7342	-70.96(3)	-39.3(4)
1936.8880	-72.75(4)	-38.5(4)
1958.9203	-69.58(4)	-41.9(2)
1990.8380	-23.12(4)	-96.2(4)
2032.7870	-68.31(3)	-39.4(4)
2069.7564	-68.27(3)	-44.2(5)
2111.6801	-35.26(3)	-81.5(4)
2113.7270	-41.95(3)	-78.3(5)
2121.6539	-55.06(3)	...
2125.6373	-59.11(3)	...
2126.6746	-61.66(3)	...
2315.9421	-18.81(3)	-102.2(8)

Table 5
(Continued)

Date KJD	RV1 (km s ⁻¹)	RV2 (km s ⁻¹)
KIC 7943602		
1704.7023	-218.7(1)	-143.2(3)
1711.7633	-145.8(1)	-231.7(6)
1741.7134	-154.1(1)	-222.2(4)
1939.9178	-217.7(1)	-144.9(3)
1958.8983	-143.3(2)	-241.8(4)
1980.8297	-223.3(1)	-138.2(5)
1990.8576	-146.5(1)	-234.3(4)
2069.7047	-228.5(1)	-132.5(6)
2111.6127	-201.9(1)	-155.0(7)
2113.6475	-228.4(1)	-131.8(4)
2125.5576	-188.7(1)	...
2126.7027	-210.3(1)	-153.2(4)
2462.6563	-172.0(2)	-198.9(5)
KIC 8054233		
1737.6793	-18.11(2)	...
1741.6890	-18.58(2)	...
1936.8672	-17.35(2)	...
1939.9853	-16.26(2)	...
1958.8028	-14.97(2)	...
1980.9473	-13.20(2)	...
2032.7695	-5.82(2)	...
2069.7403	-1.89(2)	...
2113.7753	1.15(2)	...
2121.7568	2.09(2)	...
2125.7701	2.36(2)	...
2129.6116	4.72(2)	...
2462.6225	-7.37(2)	...
2487.5853	-6.28(2)	...
KIC 8430105		
1257.8962	-1.52(2)	47.1(8)
1272.7620	0.80(2)	43.2(9)
1332.7746	-2.76(3)	...
1332.9388	-5.14(2)	...
1333.8804	-2.60(3)	...
1340.9038	8.43(5)	...
1569.8560	0.83(2)	40(2)
1591.8649	3.74(3)	38(1)
1611.9079	50.06(2)	-36(2)
1623.9504	17.79(2)	...
1704.6859	-3.85(3)	49(1)
1711.6113	-3.19(2)	47(1)
1737.7522	49.07(2)	...
1765.6598	-3.0(4)	46(2)
1936.9847	27.30(2)	-0.0(8)
1990.9240	50.95(2)	-36.3(10)
2111.6517	40.25(2)	-22.5(9)
2113.5453	46.46(3)	-30(2)
2121.5395	44.10(3)	-26(1)
2125.6213	31.29(2)	-9(1)
2126.6890	25.64(2)	-3.8(8)
2129.5366	20.33(3)	...
KIC 8702921		
1239.8587	-1.48(7)	...
1239.9301	-1.21(7)	...
1257.8566	1.54(8)	...
1272.7136	-1.28(7)	...
1332.9188	1.07(8)	...
1333.9232	1.62(8)	...

Table 5
(Continued)

Date KJD	RV1 (km s ⁻¹)	RV2 (km s ⁻¹)
1340.8599	-19.91(8)	...
1569.9025	-3.72(8)	...
1591.8791	-15.99(8)	...
1611.9427	-18.60(7)	...
1683.6718	1.95(8)	...
1737.6059	-2.25(7)	...
1741.6564	2.21(8)	...
1939.9603	-12.52(8)	...
1958.9676	-10.18(8)	...
1980.9624	-21.36(7)	...
1990.9465	0.95(8)	...
2111.7367	-1.58(7)	...
2113.6943	-8.52(7)	...
2121.6368	-17.51(7)	...
2125.7331	-1.82(8)	...
2126.7805	-0.17(8)	...
KIC 9291629		
1704.7220	-50.05(9)	-9.5(1)
1711.7861	20.76(9)	-79.9(1)
1741.7565	-80.69(9)	18.0(1)
1936.9442	12.37(8)	-73.4(1)
1958.8578	17.26(8)	-77.7(1)
1980.8990	18.53(8)	-80.1(1)
2032.6612	-79.81(8)	19.0(2)
2069.6667	-53.60(9)	-6.5(1)
2111.6369	-61.39(8)	1.1(2)
2113.6266	-78.82(8)	18.1(1)
2121.5667	-3.73(9)	-56.1(1)
2121.7727	-4.00(9)	-62.32(9)
2125.7167	17.79(8)	-80.76(10)
2126.7643	9.88(9)	-77.36(9)
2315.9212	-26.15(8)	...
KIC 9540226		
1257.9142	-25.15(2)	7.8(7)
1272.7712	-26.14(2)	7.7(4)
1332.8001	-7.65(3)	...
1332.8900	-6.28(2)	...
1333.9536	-5.28(2)	...
1340.8854	1.48(2)	-32.8(8)
1569.9639	-15.21(2)	...
1591.9752	-23.25(2)	4(3)
1623.8139	-26.23(2)	6.9(5)
1704.6592	18.43(2)	-54.1(6)
1711.6883	20.28(2)	-53.3(6)
1737.7419	-10.24(2)	...
KIC 9970396		
1569.9516	6.63(2)	-43.9(4)
1591.9628	4.21(2)	...
1611.9547	-3.76(2)	-29.9(6)
1623.8389	-10.27(2)	-23.5(2)
1697.7919	-33.74(2)	3.2(6)
1711.6722	-34.64(2)	4.1(5)
1737.5785	-30.52(2)	1.4(5)
1741.5789	-29.26(2)	0.0(4)
1939.8576	-35.19(2)	4.4(3)
1958.7833	-33.76(3)	6.5(5)
1980.8812	-27.58(2)	-0.3(6)
1990.9108	-22.65(2)	...
2032.7486	6.01(2)	...

Table 5
(Continued)

Date KJD	RV1 (km s ⁻¹)	RV2 (km s ⁻¹)
2069.7919	0.45(2)	-35.8(3)
2111.5885	-17.17(2)	...
2113.7456	-20.41(2)	...
2121.6929	-22.55(2)	-8.9(3)
2125.5948	-22.54(2)	-6.4(4)
2125.7828	-25.14(2)	-10.1(3)
2126.5730	-22.75(2)	-7.9(2)
2129.5787	-24.04(2)	-7.0(2)
2475.7632	-14.59(2)	...
2487.7494	-5.29(2)	-32.7(6)
KIC 10001167		
1569.8111	-107.32(2)	...
1591.8177	-83.34(2)	-123.8(8)
1611.8137	-84.09(2)	-123.1(7)
1623.8500	-90.59(2)	-114(2)
1648.8167	-116.85(3)	-87.3(6)
1697.7284	-95.28(2)	-110.1(6)
1711.6021	-83.61(2)	-123.7(7)
1737.5673	-86.59(2)	-122.4(7)
1741.6099	-89.97(3)	-116.0(8)
1765.5998	-113.77(2)	...
1958.7502	-82.01(3)	...
1967.9514	-82.26(2)	-123.0(9)
1980.9162	-87.70(2)	-121(1)
1990.8210	-95.77(2)	-110.1(6)
2032.6951	-130.34(2)	-74.2(9)
2111.6633	-97.47(2)	-111.2(3)
2113.6633	-99.72(2)	...
2121.5500	-106.60(2)	...
2125.5424	-111.15(2)	-97.5(8)
2129.6399	-117.27(2)	...
2286.9958	-113.77(2)	-92(1)

(This table is available in machine-readable form.)

REFERENCES

- Alam, S., Albareti, F. D., Allende, C., et al. 2015, *ApJS*, **219**, 12
- Allard, F., Homeier, D., & Freytag, B. 2011, in ASP Conf. Ser. 448, 16th Cambridge Workshop on Cool Stars, Stellar Systems, and the Sun, ed. C. Johns-Krull, M. K. Browning, & A. A. West (San Francisco, CA: ASP), 91
- Baines, E. K., Armstrong, J. T., Schmitt, H. R., et al. 2014, *ApJ*, **781**, 90
- Beck, P. G., Hambleton, K., Vos, J., et al. 2014, *A&A*, **564**, A36
- Beck, P. G., Hambleton, K., Vos, J., et al. 2015, EPJ Web of Conferences, 101, 06004
- Bedding, T. R., Mosser, B., Huber, D., et al. 2011, *Natur*, **471**, 608
- Belkacem, K., Goupil, M. J., Dupret, M. A., et al. 2011, *A&A*, **530**, A142
- Belkacem, K., Samadi, R., Mosser, B., Goupil, M.-J., & Ludwig, H.-G. 2013, in ASP Conf. Ser. 479, Progress in Physics of the Sun and Stars: A New Era in Helio- and Asteroseismology, ed. H. Shibahashi & A. E. Lynas-Gray (San Francisco, CA: ASP), 61
- Bender, C. F., Mahadevan, S., Deshpande, R., et al. 2012, *ApJL*, **751**, L31
- Brogaard, K., Jessen-Hansen, J., Handberg, R., et al. 2016, arXiv:1601.01412
- Broomhall, A.-M., Chaplin, W. J., Davies, G. R., et al. 2009, *MNRAS*, **396**, L100
- Brown, T. M., Latham, D. W., Everett, M. E., & Esquerdo, G. A. 2011, *AJ*, **142**, 112
- Castelli, F., & Kurucz, R. L. 2004, arXiv:astro-ph/0405087
- Chaplin, W. J., Kjeldsen, H., Christensen-Dalsgaard, J., et al. 2011, *Sci*, **332**, 213
- Chaplin, W. J., & Miglio, A. 2013, *ARA&A*, **51**, 353
- Chiappini, C., Anders, F., Rodrigues, T. S., et al. 2015, *A&A*, **576**, L12
- Christensen-Dalsgaard, J. 2012, *AN*, **333**, 914

- Claret, A., Hauschildt, P. H., & Witte, S. 2012, *A&A*, **546**, A14
- Corsaro, E., & De Ridder, J. 2014, *A&A*, **571**, A71
- Corsaro, E., De Ridder, J., & García, R. A. 2015, *A&A*, **579**, A83
- Eisenstein, D. J., Weinberg, D. H., Agol, E., et al. 2011, *AJ*, **142**, 72
- Epstein, C. R., Elsworth, Y. P., Johnson, J. A., et al. 2014, *ApJL*, **785**, L28
- Frandsen, S., Lehmann, H., Hekker, S., et al. 2013, *A&A*, **556**, A138
- Fuller, J., Cantiello, M., Stello, D., García, R. A., & Bildsten, L. 2015, *Sci*, **350**, 423
- Gaulme, P., Appourchaux, T., & Boumier, P. 2009, *A&A*, **506**, 7
- Gaulme, P., Jackiewicz, J., Appourchaux, T., & Mosser, B. 2014, *ApJ*, **785**, 5
- Gaulme, P., McKeever, J., Rawls, M. L., et al. 2013, *ApJ*, **767**, 82
- Guggenberger, E., Hekker, S., Basu, S., & Bellinger, E. 2016, *MNRAS*, arXiv:1606.01917
- Hekker, S., Debosscher, J., Huber, D., et al. 2010, *ApJL*, **713**, L187
- Hekker, S., Elsworth, Y., Basu, S., et al. 2013, *MNRAS*, **434**, 1668
- Helminiak, K. G., Ukita, N., Kambe, E., & Konacki, M. 2015, *ApJL*, **813**, L25
- Holtzman, J. A., Shetrone, M., Johnson, J. A., et al. 2015, *AJ*, **150**, 148
- Huber, D. 2014, arXiv:1404.7501
- Huber, D., Bedding, T. R., Stello, D., et al. 2011, *ApJ*, **743**, 143
- Huber, D., Ireland, M. J., Bedding, T. R., et al. 2012, *ApJ*, **760**, 32
- Huber, D., Silva Aguirre, V., Matthews, J. M., et al. 2014, *ApJS*, **211**, 2
- Kallinger, T., Hekker, S., Mosser, B., et al. 2012, *A&A*, **541**, A51
- Kallinger, T., Mosser, B., Hekker, S., et al. 2010, *A&A*, **522**, A1
- Kjeldsen, H., & Bedding, T. R. 1995, *A&A*, **293**, 87
- Magrini, L., Randich, S., Friel, E., et al. 2013, *A&A*, **558**, A38
- Martig, M., Rix, H.-W., Silva Aguirre, V., et al. 2015, *MNRAS*, **451**, 2230
- Mazeh, T., & Zucker, S. 1994, *Ap&SS*, **212**, 349
- Miglio, A., Brogaard, K., Stello, D., et al. 2012, *MNRAS*, **419**, 2077
- Miglio, A., Chiappini, C., Morel, T., et al. 2013, *MNRAS*, **429**, 423
- Mosser, B., & Appourchaux, T. 2009, *A&A*, **508**, 877
- Mosser, B., Belkacem, K., Goupil, M. J., et al. 2011, *A&A*, **525**, L9
- Mosser, B., Goupil, M. J., Belkacem, K., et al. 2012, *A&A*, **548**, A10
- Mosser, B., Michel, E., Belkacem, K., et al. 2013, *A&A*, **550**, A126
- Nidever, D. L., Holtzman, J. A., Allende, C., et al. 2015, *AJ*, **150**, 173
- Pietrinferni, A., Cassisi, S., Salaris, M., & Castelli, F. 2004, *ApJ*, **612**, 168
- Pinsonneault, M. H., An, D., Molenda-Zakowicz, J., et al. 2012, *ApJS*, **199**, 30
- Pinsonneault, M. H., Elsworth, Y., Epstein, C., et al. 2014, *ApJS*, **215**, 19
- Rawls, M. L., Gaulme, P., McKeever, J., et al. 2016, *ApJ*, **818**, 108
- Sharma, S., Stello, D., Bland-Hawthorn, J., Huber, D., & Bedding, T. R. 2016, arXiv:1603.05661
- Silva Aguirre, V., Casagrande, L., Basu, S., et al. 2012, *ApJ*, **757**, 99
- Sing, D. K. 2010, *A&A*, **510**, A21
- Snedden, C., Bean, J., Ivans, I., Lucatello, S., & Sobeck, J. 2012, *MOOG: LTE Line Analysis and Spectrum Synthesis*, Astrophysics Source Code Library, ascl:1202.009
- Sousa, S. G. 2014, arXiv:1407.5817
- Sousa, S. G., Santos, N. C., Adibekyan, V., Delgado-Mena, E., & Israelian, G. 2015, *A&A*, **577**, A67
- Sousa, S. G., Santos, N. C., Israelian, G., Mayor, M., & Monteiro, M. J. P. F. G. 2007, *A&A*, **469**, 783
- Southworth, J. 2013, *A&A*, **557**, A119
- Stello, D., Cantiello, M., Fuller, J., et al. 2016, *Natur*, **529**, 364
- Stello, D., Chaplin, W. J., Bruntt, H., et al. 2009, *ApJ*, **700**, 1589
- Tassoul, M. 1980, *ApJS*, **43**, 469
- Tsantaki, M., Sousa, S. G., Adibekyan, V. Z., et al. 2013, *A&A*, **555**, A150
- White, T. R., Bedding, T. R., Gruberbauer, M., et al. 2012, *ApJL*, **751**, L36
- White, T. R., Bedding, T. R., Stello, D., et al. 2011, *ApJ*, **743**, 161
- White, T. R., Huber, D., Maestro, V., et al. 2013, *MNRAS*, **433**, 1262